Characterizing the mechanical response of metallic glasses to uniaxial tension using a spring network model

Aya Nawano [ORCID],[1] Weiwei Jin [ORCID],[1] Jan Schroers [ORCID],[1] Mark D. Shattuck [ORCID],[2] and Corey S. O'Hern [ORCID][1,3,4,5,*]

[1]*Department of Mechanical Engineering and Materials Science, Yale University, New Haven, Connecticut 06520, USA*
[2]*Benjamin Levich Institute and Physics Department, The City College of New York, New York, New York 10031, USA*
[3]*Department of Physics, Yale University, New Haven, Connecticut 06520, USA*
[4]*Department of Applied Physics, Yale University, New Haven, Connecticut 06520, USA*
[5]*Graduate Program in Computational Biology and Bioinformatics, Yale University, New Haven, Connecticut 06520, USA*

A coarse-grained spring network model is proposed for the prediction of the mechanical response of metallic glasses as a function of the microstructure prior to loading. This model describes the mechanical response of metallic glasses using a network of parallel springs that can break and reform, mimicking atomic rearrangements during deformation. We compare predictions of the spring network model for stress versus strain to results from numerical simulations of athermal quasistatic, uniaxial tensile deformation of $Cu_{50}Zr_{50}$ metallic glasses using Lennard-Jones (LJ) and embedded atom method (EAM) atomic interactions. We show that both the LJ and EAM models possess qualitatively similar stress σ versus strain γ curves. By specifying five parameters [ultimate strength, strain at ultimate strength, slopes of $\sigma(\gamma)$ at $\gamma = 0$ and at large strain, and strain at fracture where $\sigma = 0$], we demonstrate that the spring network model can accurately describe the form of the stress-strain curves during uniaxial tension for the computational studies of $Cu_{50}Zr_{50}$, as well as recent experimental studies of several Zr-based metallic glasses.

I. INTRODUCTION

Bulk metallic glasses are alloys with amorphous atomic structure. Since they possess larger values for the strength and elastic limit compared to those for conventional crystalline alloys, they represent a promising class of structural materials [1]. Tensile loading is a common and important loading geometry for understanding the mechanical response of metallic glasses [2–10]. Under tensile loading, metallic glasses at room temperature are typically brittle. Shear bands, or localized regions of large strain, form during deformation that can lead to failure of the material [2]. As an example of this behavior, in Fig. 1(a), we show the engineering stress σ versus engineering strain γ from recent experiments that perform uniaxial tension tests on sputtered ZrNiAl metallic glasses [3]. The more ductile sample has an ultimate strength of $\sigma_m \sim 1.5$ GPa and fractures at $\gamma_f \sim 11.6\%$, whereas the more brittle sample has an ultimate strength of $\sigma_m \sim 1.7$ GPa and fractures at $\gamma_f \sim 8\%$. The two samples were fabricated using similar processes, but the more brittle sample was annealed at a temperature below the glass transition temperature T_g for 24 hours after fabrication. Many factors have been shown to affect the tensile plasticity of metallic glasses, such as the cooling history [4], sample size [3,5–7], strain rate [8–10], and temperature [9,10] at which the testing occurs. In general, larger samples, samples prepared at lower cooling rates, and samples tested at lower temperatures are more brit-

tle. In addition, experiments on bending and compression of metallic glasses have shown that their mechanical response is influenced by changes in chemical composition [11–13]. For example, adding 5% of Al atoms into $Cu_{50}Zr_{50}$ bulk metallic glasses increased the failure strain from 7.9% to 18% in compression tests [13]. Also, Pd-based bulk metallic glasses were found to be brittle when formed at low cooling rates, whereas Pt-based bulk metallic glasses are ductile regardless of the cooling rate used to prepare the samples [11]. Because there are so many factors that influence the microstructure of metallic glasses, it is difficult to predict the mechanical response of metallic glasses to applied deformations.

The mechanical response of metallic glasses is controlled by the atomic interactions and motions that arise from applied deformations. Numerous molecular dynamics (MD) simulation studies have shown that the mechanical response of metallic glasses to applied deformations involves highly collective and nonaffine atomic motions that are spatially and temporally correlated [14–25]. To understand the mechanical response of metallic glasses at larger length scales, coarse-grained mesoscale models have been developed [18,26–28]. For example, elastoplastic models consider metallic glasses as a collection of mesoscopic elements, where each element deforms elastically until it reaches its local yield strain [26,29–31]. After yielding, the elements redistribute their stress to neighboring elements and the stress is reset to the largest value in the elastic state. Further, elaborations of elastoplastic models have coupled the shape of the yield strain distributions to the evolving microstructure during applied deformation [32]. Several studies have shown

*corey.ohern@yale.edu

that elastoplastic models can describe the stress-strain curves for model Lennard-Jones (LJ) glasses undergoing simple shear over a range of strain rates [32–34].

Theoretical models for the irreversible atomic motions that occur during applied deformation can be used to improve elastoplastic descriptions of metallic glasses. For example, the plastic strain can be calculated by identifying shear transformation zones (STZs), or groups of atoms that undergo collective, nonaffine motion in response to applied deformations [18,24,35–41]. Manning *et al.* [42] derived a system of ordinary differential equations (ODEs) for the deviatoric stress and an effective temperature that controls the STZ density in computational studies of LJ glasses undergoing simple shear. The system of ODEs includes seven parameters, such as the initial and steady-state effective temperature, characteristic size of an STZ, and effective temperature diffusivity, which are chosen so that the predicted stress versus strain and degree of strain localization match the behavior in the numerical simulations. Similar studies have coupled elastoplastic and STZ descriptions to describe the stress versus strain in molecular dynamics simulations of embedded atom method potentials for $Cu_{50}Zr_{50}$ undergoing simple shear [43].

Free volume descriptions have also been employed to predict the stress versus strain curves for metallic glasses undergoing homogeneous deformation near the glass transition temperature [44–46]. Parameters in this model are determined by performing deformation studies at several different strain rates. The free volume model has been able to recapitulate the stress versus strain curves for Zr-based metallic glasses undergoing compression over a range of strain rates. However, the free volume model has not been generalized so that it can describe serrated stress versus strain curves associated with shear localization or brittle fracture. Serrated stress versus strain curves are frequently observed in experimental studies of metallic glasses deformed at temperatures well below the glass transition temperature and at low strain rates [47–49].

The fiber bundle model [50–52] was originally developed to describe fibrous materials under tension, but it has also been used to describe amorphous solids undergoing tensile loading [53,54]. The fiber bundle model is a coarse-grained, one-dimensional model that considers fibers in parallel under a constant load. An individual fiber breaks when its extension exceeds a randomly selected cutoff, and its load is then redistributed to neighboring fibers. This model displays brittle, quasibrittle, and ductile failure modes as a function of the heterogeneity in the failure thresholds and the length scale over which the stress is redistributed after local failure [53]. Key differences between the fiber bundle and elastoplastic models are that each fiber only experiences elastic deformation before yielding and there is no stress recovery within a fiber after it yields.

In this article, we develop a spring network model to describe the mechanical response of metallic glasses to tensile loading. We use this model to describe the mechanical response from numerical simulations of $Cu_{50}Zr_{50}$ glasses undergoing athermal, quasistatic tension tests, as well as experimental studies of several Zr-based metallic glasses undergoing tensile loading at finite temperature [3,6,10]. The binary alloy $Cu_{50}Zr_{50}$ is chosen for the numerical simulations as it is one of the few binary alloys that form bulk metallic

glasses [55] with a critical cooling rate of $R_c \sim 250$ K/s [56]. The spring network model includes a large number N_s of initially unstretched springs in parallel prior to the applied deformation. Similar to the fiber bundle model, the springs break when their stretching exceeds a cutoff. However, unlike the conventional fiber bundle model, at each strain step, new springs form, contributing to the stress that resists the tensile load. In the $N_s \to \infty$ limit, we derive an analytical form for the stress σ versus strain γ for the spring network model undergoing tensile loading. This expression includes five important parameters: the ultimate strength, strain at which this occurs, slopes of $\sigma(\gamma)$ at zero and at large strain, and failure strain at which $\sigma = 0$. This expression for $\sigma(\gamma)$ accurately describes the mechanical response of both Lennard-Jones (LJ) and embedded atom method (EAM) models for $Cu_{50}Zr_{50}$ metallic glasses under athermal, quasistatic tension tests. Furthermore, we also show that $\sigma(\gamma)$ obtained from the spring network model can accurately describe the mechanical response of several Zr-based metallic glasses, including $Zr_{65}Al_{10}Ni_{10}Cu_{15}$, $Zr_{56}Ni_{22}Al_{22}$, and $Cu_{49}Zr_{51}$ at finite temperature and nonzero strain rate, obtained in recent experimental studies [3,6,10]. Even though the differences in system size, temperature, and strain rate between the simulation and experimental studies give rise to key differences in the stress versus strain curves, the spring network model (with different sets of parameters) can accurately recapitulate their stress versus curves. These results emphasize the versatility and generality of the spring network model.

II. METHODS

In this section, we first introduce the cooling and structural relaxation protocols to prepare $Cu_{50}Zr_{50}$ metallic glasses with different amounts of local positional order in the numerical simulations. We also describe the simulation method for applying the tensile deformation to the metallic glass samples. We then present the spring network model, derive an analytical expression for the stress versus strain $\sigma(\gamma)$, and relate the five parameters in the spring network model to important features of $\sigma(\gamma)$.

A. Generating metallic glasses with different amounts of positional order

We focus on $Cu_{50}Zr_{50}$ systems modeled using Lennard-Jones (LJ) and embedded atom method (EAM) atomic interactions (see Appendix A). Each system contains $N = 3456$ atoms confined within a cuboidal box with periodic boundary conditions in the x, y, and z directions. We show in Appendix B that above this system size $\sigma(\gamma)$ is insensitive to N for all preparation protocols. Several previous numerical studies have shown that it is difficult for metallic glass samples with small aspect ratios (defined as the ratio between the initial sample length along the deformation direction to the initial length in directions perpendicular to deformation to form shear bands [57–59]). We chose aspect ratios $L_z/L_x = 1/2$ and $L_z/L_y = 1/2$ to avoid large-scale shear-band formation that leads to catastrophic failure in the numerical simulations. (Note that tensile loading is applied in the z direction.) For $Cu_{50}Zr_{50}$ metallic glasses, we verify in Appendix C that

samples with larger initial aspect ratios and prepared using slow cooling rates display shear banding when they are subjected to athermal, quasistatic tensile loading.

To prepare the metallic glass samples, we first equilibrated the systems at high temperature above the melting temperature, $T > T_m$, and then cooled them linearly to low temperature $T_0 < 1$ K at constant low pressure P_0 that is several orders of magnitude below the maxima in the shear stress versus strain curves (obtained from uniaxial tension) using the Nosé-Hoover thermostat and barostat. The equations of motion are integrated using a modified velocity-verlet algorithm with time step $\Delta t = 10^{-3}$ ps. The cooling rates spanned four orders of magnitude from 10^{10} to 10^{14} K/s, but remain much larger than the critical cooling rate $R_c \sim 250$ K/s for $Cu_{50}Zr_{50}$. After thermally quenching the samples, they were decompressed and potential energy minimized using the conjugate gradient method to reach $P = P_0$ and zero temperature. The maximum total force on an atom after potential energy minimization was 10^{-10} eV/Å. We also performed instantaneous thermal quenches by equilibrating the systems at $T > T_m$ and then minimizing the total potential energy at a constant volume that corresponds to $P = P_0$.

We performed the thermal quenching studies at different cooling rates so that we can explore the mechanical response of $Cu_{50}Zr_{50}$ metallic glasses with different degrees of ductility. In addition to thermally quenched glasses, we also generated disordered face-centered cubic (FCC) structures to further enhance the ductility of the metallic glass samples under uniaxial tensile deformation. We first placed Zr and Cu atoms randomly on an FCC lattice (while maintaining the correct stoichiometry for $Cu_{50}Zr_{50}$) followed by potential energy minimization. The FCC lattice is unstable for random mixtures of Cu and Zr, and thus potential energy minimization induces positional disorder. [Note that pure Cu forms FCC and pure Zr forms hexagonal close packed (HCP) crystalline structures.]

B. Athermal, quasistatic uniaxial tension

After generating the $Cu_{50}Zr_{50}$ metallic glass samples, we perform athermal, quasistatic uniaxial tension tests. In particular, we apply successive small uniaxial strain steps of $\delta\gamma = 10^{-4}$ along the z direction by increasing the sample length from its current value L_z to $L_z' = L_z + \Delta L_z$ and shifting the z positions of the atoms affinely such that $z_i' = z_i(1 + \delta\gamma)$ [as shown in the inset of Fig. 1(b)]. Each strain step is followed by potential energy minimization. $\Delta L_z = L_{z0}\delta\gamma$ and L_{z0} is the original length of the sample in the z direction. Before applying the tensile deformations, we open the boundaries in the x and y directions to allow necking of the sample. To remove the residual stress caused by opening the boundaries, we apply athermal, quasistatic tension or compression in the z direction until the engineering stress is zero. We then apply athermal, quasistatic tensile deformation in small strain steps until the total strain reaches $\gamma = 1$.

C. Calculating the engineering stress

During uniaxial tensile deformation, the thickness of the metallic glasses becomes length dependent due to necking of the sample. The true stress is defined as the total force in the
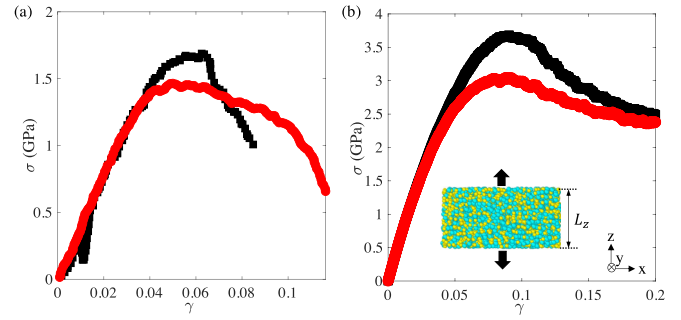

FIG. 1. Engineering stress σ plotted vs engineering strain γ from (a) experiments and (b) simulations of metallic glasses undergoing uniaxial tension. The data in (a) is from sputtered $Zr_{56}Ni_{22}Al_{22}$ metallic glasses [3] with (black) and without (red) annealing at temperatures below the glass transition for 24 hours. The data in (b) is from athermal, quasistatic uniaxial tension simulations of $Cu_{50}Zr_{50}$ modeled using EAM interactions generated at cooling rates $R = 10^{10}$ K/s (black) and 10^{13} K/s (red) and averaged over 50 samples. The inset shows the geometry used in the simulations. The samples have periodic boundaries in the z direction that are moved vertically to apply tensile deformations and open boundaries in the x and y directions.

z direction divided by the cross-sectional area of the sample at each strain. Thus, the true stress is difficult to calculate since we would need to accurately describe the surface of the deformed sample. In contrast, the engineering stress is defined as the total force in the z direction divided by the undeformed cross-sectional area, which is nearly uniform over the length of the sample. We show typical engineering stress versus strain curves for thermally quenched $Cu_{50}Zr_{50}$ metallic glasses modeled using the EAM potential in Fig. 1(b).

To calculate the engineering stress, we consider the total force in the z direction crossing the x-y plane in the sample [60,61] at $z = z'$. Note that any x-y plane in the sample gives the same total force in the z direction because the system is in force balance. The total force in the z direction crossing the z' plane is

$$F_{zz'} = \sum_{i,j} F_{ijz}, \qquad (1)$$

where F_{ijz} is z component of the force $\vec{F}_{ij}$ on atom i from other atoms j, and the sum only includes atom pairs i and j such that $\vec{r}_{ij}$ intersects the plane $z = z'$. Since $\vec{F}_{ij} = -\vec{F}_{ji}$, the sum of F_{ijz} only includes the force on atom i or j that has the lower z-coordinate than the other atom. We define our coordinate system such that $-L_z/2 \leqslant z \leqslant L_z/2$, and thus we set $z' = 0$. Since $L_z/2 > r_c$ for both the LJ and EAM models, atoms only interact across the plane $z' = 0$ and not through the periodic image cells. The total force in the z direction across the plane $z' = 0$ is the z component of the total force on atoms in the lower region ($z' < 0$) arising from interactions with atoms in the upper region ($z' > 0$).

For LJ interactions, $\vec{F}_{ij} = -(dU/dr_{ij})\hat{r}_{ij}$. For EAM interactions, the force on atom i from j is

$$\vec{F}_{ij} = -\big[(\partial\mathcal{F}_i/\partial\rho_i)(\partial\rho_i/\partial r_{ij}) + (\partial\mathcal{F}_j/\partial\rho_j)(\partial\rho_j/\partial r_{ij}) \\ + \big(\partial\phi_{ij}^p/\partial r_{ij}\big)\big]\hat{r}_{ij}, \qquad (2)$$
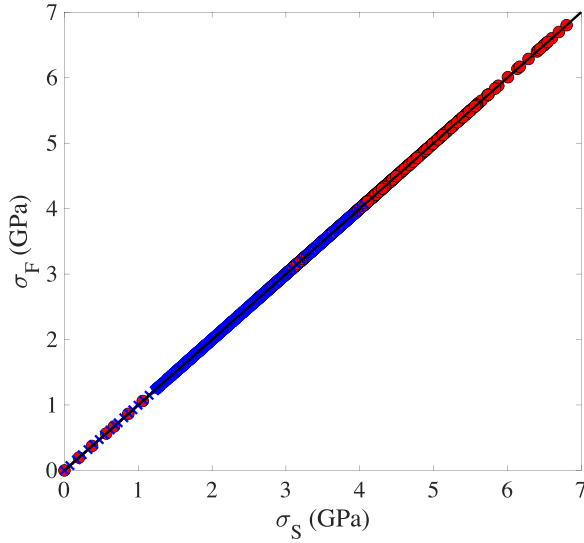
FIG. 2. Two definitions of the engineering stress $\sigma_F = F_{zz'}L_z/A_0$ and $\sigma_S = S_{zz}/A_0$ plotted against each other. $F_{zz'}$ is the total force in the z direction crossing the z' plane [Eq. (1)] and S_{zz} is the zz contribution to the virial S_{zz} [Eq. (3)]. A_0 is the undeformed area of the sample and L_z is its length in the z direction. Data from uniaxial tension tests on $Cu_{50}Zr_{50}$ modeled using LJ (red circles) and EAM interactions (blue crosses) are included. The solid black line indicates that $\sigma_F = \sigma_S$.

which includes two additional terms arising from the embedding function $\mathcal{F}_i$ and where $\rho_i = \sum_{j \neq i} \rho_{ij}(r_{ij})$ is the electron density of atom i at position $\vec{r}_i$ and ϕ_{ij}^p is the EAM pair potential energy function. We then define the engineering stress, $\sigma_F = F_{zz'}/A_0$, where A_0 is the cross-sectional area of the undeformed sample. We first determine the α shape of the undeformed sample, and then calculate its volume V_0 and $A_0 = V_0/L_{z0}$. We find that the relative fluctuations in A_0 are less than 0.6% for all preparation protocols and both LJ and EAM interactions.

We also compared the results for σ_F to the results for the engineering stress obtained using the zz component of the virial stress tensor,

$$S_{zz} = \sum_{i=1}^{N} z_i F_{iz}. \quad (3)$$

In terms of S_{zz}, the engineering stress is defined as

$$\sigma_S = \frac{S_{zz}}{L_{z0}A_0}. \quad (4)$$

In Fig. 2, we show that, as expected, $\sigma_F = \sigma_S$ for uniaxial tension applied to $Cu_{50}Zr_{50}$ metallic glass samples modeled using the LJ and EAM interactions. Below, we use $\sigma \equiv \sigma_F$ to display the engineering stress.

D. Spring network model

We now describe the key elements of the spring network model, which are illustrated in Fig. 3. In the undeformed state at $\gamma = 0$, the sample is in mechanical equilibrium, the atoms are in their equilibrium positions with an initial set of nearest (Voronoi) neighbors, and the engineering stress σ is zero. As
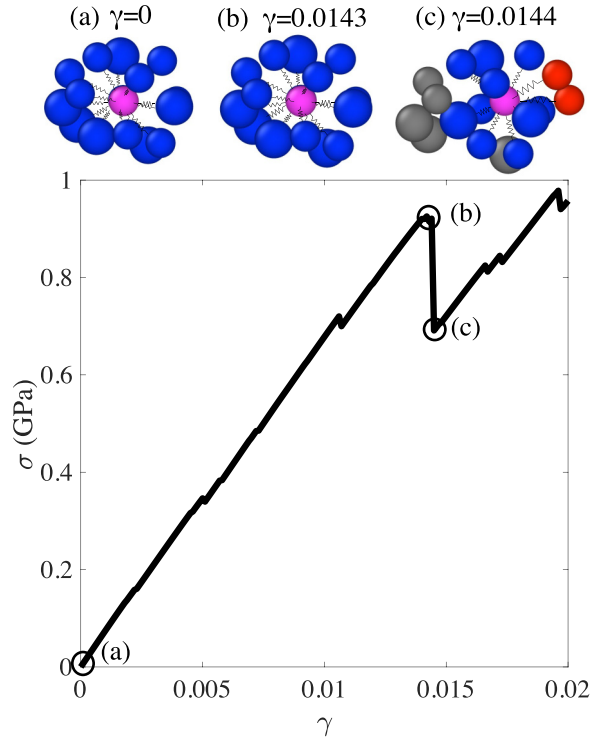

FIG. 3. Engineering stress σ as a function of strain γ from a uniaxial tension test of a $Cu_{50}Zr_{50}$ sample generated using the EAM model at cooling rate $R = 10^{10}$ K/s. The local regions in the three insets (a)–(c), which show the nearest (Voronoi) neighbors of a specified central atom (magenta), are taken from systems with total engineering stress labeled (a)–(c) in the main plot. Between total strain (a) $\gamma = 0$ and (b) 0.0143, there is no change in the (blue) nearest neighbors of the selected central atom. After a large atomic rearrangement event at (c) $\gamma = 0.0144$, some of the atoms that were nearest neighbors of the central atom in (a) and (b) are no longer nearest neighbors (grey). The central atom also gains new nearest neighbors (red) that were not nearest neighbors at $\gamma = 0$.

the uniaxial strain γ is applied, σ increases roughly linearly. Small drops in σ occur prior to point (b), but the nearest neighbors of the selected central atom remain the same as they were at $\gamma = 0$. Between points (b) and (c), a large engineering stress drop occurs, which corresponds to an atomic rearrangement event where five atoms are no longer nearest neighbors of the central atom, and two new atoms become nearest neighbors of the central atom. Changes in the nearest neighbors of atoms can occur throughout the sample and at various strain steps during uniaxial tension deformation. Inspired by these atomic rearrangement events, we develop a mesoscopic one-dimensional spring network model that considers the breaking and forming of springs in parallel during deformation. The breaking (formation) of a spring represents a loss (gain) of nearest-neighbor atoms in a local region. The total force (in the z direction) resisting the extension of the sample will be related to the number of springs at each strain step and how much each spring is stretched. Our goal is to develop a simple model with a small number of parameters, yet we want it to possess a sufficient number of parameters so that it is able to quantitatively characterize the mechanical response of metallic glasses.
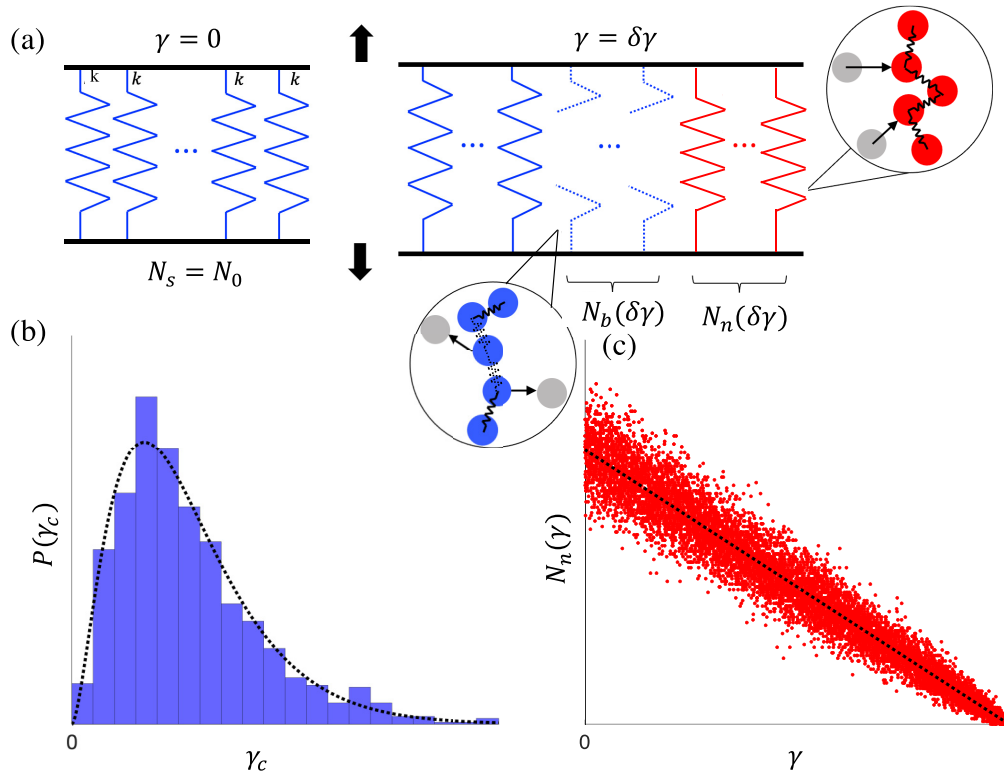
FIG. 4. (a) Schematic of the spring network model. In the undeformed sample at $\gamma = 0$, $N_s = N_0$ identical springs are initially connected in parallel with spring constant k and can transmit force in the (vertical) pulling direction. After a single step in uniaxial strain $\gamma = \delta\gamma$, $N_b(\delta\gamma)$ springs break according to each spring's cutoff strain γ_c, which is drawn randomly from a Gamma distribution. The breaking of a spring, which represents an atomic rearrangement event (atoms change color from blue to gray), prevents that spring from transmitting force in the pulling direction. Also, during an atomic rearrangement event, $N_n(\delta\gamma)$ springs can form and begin to transmit force (atoms change color from gray to red). (b) The probability distribution of spring breaking cutoff strains $P(\gamma_c)$, which converges to a Gamma distribution in the $N_0 \to \infty$ limit (dotted line). In this example, the two parameters for $P(\gamma_c)$ are $\alpha = 2.7$ and $\beta = 0.02$. (c) The number of new springs $N_n(\gamma)$ as a function of strain γ. At each strain, $N_n(\gamma) \sim N_n^p(\gamma)p$ springs form on average, where $N_n^p(\gamma)$ is the number of potential new springs that can form and p is the probability that these new springs are instantiated. We show data for $p = 0.1$ and $N_n^p(\delta\gamma) = 10^3$. In the $N_n^p \to \infty$ limit, $N_n(\gamma)$ converges to the black dotted line with vertical intercept $pN_n^p(\delta\gamma)$ and slope $p(dN_n^p/d\gamma)$.

The spring network model is summarized in Fig. 4(a). Initially, we assume that there are $N_s = N_0$ identical, unstretched springs in parallel, each with spring constant k and rest length l_0. After each applied step strain, we assume that all springs experience the same amount of strain $\delta\gamma$. Thus, the force experienced by spring j after a total strain γ^j is $F^j = kl_0\gamma^j$. Each spring is assigned a cutoff strain $\gamma_c > 0$, which is the total strain at which the spring breaks. Numerical simulations of strained and unstrained glasses suggest that the mean value of the strain $\langle\gamma_c\rangle$ at which the first plastic event occurs, decreases as a power law with the increasing number of atoms N: $\langle\gamma_c\rangle \sim N^{-0.6}$ [62,63]. Hence, these numerical simulations suggest that in the spring network model, we should choose a distribution $P(\gamma_c)$ such that $\langle\gamma_c\rangle \to 0$ in the $N_s \to \infty$ limit. Furthermore, it has been shown that the distribution of the critical strains, at which the first plastic event occurs (i.e., the weakest spring in the spring network model), obeys a Weibull distribution [62]. However, in the spring network model, we not only consider the first plastic event, but the plastic events at all strains during the tension tests. We assume that the cutoff strain of *individual* springs follows an exponential distribution and that an integer number α of springs break within a set of N_s springs simultaneously. The distribution of the sum of an

integer number α of independent and identically distributed random cutoff strains gives an Erlang distribution function, i.e., the Gamma distribution with integer shape parameter α. When considering an ensemble of initial samples, the integer α can vary from sample to sample. For a noninteger average α, $P(\gamma_c)$ becomes a Gamma distribution. Therefore, γ_c is randomly selected from a Gamma distribution,

$$P(\gamma_c) = \frac{\beta^\alpha}{\Gamma(\alpha)}\gamma_c^{\alpha-1}e^{-\beta\gamma_c}, \quad (5)$$

where $\Gamma(.)$ is the Gamma function. $P(\gamma_c)$ has two parameters, the shape parameter α and rate parameter β, that give rise to the mean α/β and variance α/β^2 [see Fig. 4(b)]. Selecting cutoff strains from $P(\gamma_c)$ gives a coarse-grained representation of the structural disorder in metallic glasses, such as fluctuations in the values of $\vec{r}_{ij} \cdot \hat{z}$ for interacting atomic pairs. When a given spring breaks, the force on that spring is set to zero.

At each strain step, new springs can also form. We assume that the number of potential new springs decreases linearly with the total strain,

$$N_n^p(\gamma_n) = N_n^p(\delta\gamma) - \frac{dN_n^p}{d\gamma}\gamma_{n-1}, \quad (6)$$

where $\gamma_n = n\delta\gamma$ is the total strain after n strain steps. This form for $N_n^p(\gamma_n)$ is consistent with the fact that the cross-sectional area decreases with increasing uniaxial strain, and thus there are fewer atoms in the transverse direction for forming new spring connections. [We also considered quadratic and piecewise linear functions for $N_n^p(\gamma_n)$, which include an additional parameter. However, the form in Eq. (6) provided high-quality fits to the data from simulations of athermal, quasistatic uniaxial tension.] The *potential* new springs form instantiated new springs with probability p. The scatter plot in Fig. 4(c) shows the number of new springs $N_n(\gamma_n) = pN_n^p(\gamma_n)$ as a function of total strain γ_n for $p = 0.1$ and $N_n^p(\delta\gamma) = 10^3$. When a new spring is formed, it is initiated with the same rest length l_0 and γ_c is randomly selected from the same $P(\gamma_c)$ regardless of the total strain. Newly formed springs also experience the same incremental strain $\delta\gamma$ at each applied strain step.

The total force of the spring network at total strain $\gamma_n = n\delta\gamma$ is

$$F_s(\gamma_n) = \sum_{j=1}^{N_s} kl_0\gamma_n^j, \tag{7}$$

where γ_n^j is the total strain experienced by the jth spring after n strain steps applied to the initial undeformed sample, which differs from the total strain γ_n for springs that were not present at $\gamma = 0$. Thus, to calculate the total force for the spring network model at γ_n, we need to track the number of initial springs that are still intact at γ_n, the number of new springs that have formed since $\gamma = 0$, and at what strains each of these new springs form.

The engineering stress versus strain curve $\sigma(\gamma)$ for uniaxial tension for a single $Cu_{50}Zr_{50}$ metallic glass sample using the EAM model with $N = 3456$ atoms includes numerous rapid drops in stress as shown in Fig. 3. Several studies have shown that for metallic glasses undergoing athermal, quasistatic deformation, the size of the stress drops decreases and the number of stress drops increases with increasing system size. To mimic the large-system limit, we can calculate the ensemble-averaged $\sigma(\gamma)$ from the numerical simulations of the LJ and EAM models over many realizations. The results for $\sigma(\gamma)$ from the spring network model in the large-system limit can be obtained by taking the limits $N_s \to \infty$ and $N_n^p \to \infty$. In this limit, we can derive an analytical expression for the total force in the spring network model [Eq. (7)], and compare it to $\sigma(\gamma)A_0$ obtained from the athermal, quasistatic tension tests of $Cu_{50}Zr_{50}$ samples modeled using the LJ and EAM interaction potentials.

If N_0 springs are initialized at $\gamma = 0$, the number of these springs that have not broken after strain γ_n is $N(\gamma_n) = N_0[1 - C(\gamma_n)]$, where $C(\gamma_n)$ is the cumulative distribution function for the Gamma distribution. Since these springs experience the same total strain, we can calculate the total force from the remaining springs at γ_n,

$$F_{s0}(\gamma_n) = kl_0\gamma_nN_0[1 - C(\gamma_n)]. \tag{8}$$

In the limit $N_n^p \to \infty$, the number of new springs that form $N_n(\gamma_n)$ can also be derived. Using Eq. (6), we find

$$N_n(\gamma_n) = pN_n^p(\gamma_n) = N_n(\delta\gamma) - \frac{dN_n}{d\gamma}\gamma_{n-1}. \tag{9}$$

To calculate the total force from the newly formed springs, we need to take into account the fact that $N_n(\gamma_n)$ new springs are generated at γ_n and these springs break after an additional strain of γ_c, which is selected randomly from a Gamma distribution. The total force arising from the new springs at γ_n is

$$F_{sn}(\gamma_n) = kl_0\sum_{i=0}^{n-1}\left(N_n(\delta\gamma) - \frac{dN_n}{d\gamma}(\gamma_{n-1} - \gamma_i)\right)\gamma_i[1 - C(\gamma_i)], \tag{10}$$

where $F_{sn}(\gamma_0) = 0$. Thus, the total force in the spring network at strain γ_n is given by

$$F_s(\gamma_n) = F_{s0}(\gamma_n) + F_{sn}(\gamma_n), \tag{11}$$

where F_{s0} and F_{sn} are provided in Eqs. (8) and (10), respectively. Taking the continuum limit in strain and normalizing the spring force by the sample's undeformed cross-sectional area A_0 allow a comparison to the engineering stress versus strain obtained in the simulations of athermal, quasistatic uniaxial tensile deformations,

$$\sigma_s(\gamma) = F_s(\gamma)/A_0. \tag{12}$$

E. Comparison of the predictions of the spring network model and results from atomistic simulations

The engineering stress σ_s in Eq. (12) from the spring network model has five parameters. These include the number of initial springs N_0, number of new springs that are formed during the first strain step $N_n(\delta\gamma)$, and the change in the number of new springs that are formed per strain step $dN_n/d\gamma$. In addition, the cumulative distribution $C(.)$ that controls the cutoff strain is characterized by two parameters, α and β. Motivated by $\sigma(\gamma)$ from experiments and simulations of uniaxial tension of metallic glasses in Fig. 1, we can now relate these five parameters from the spring network model to five key features of the shape of the engineering stress versus strain curve illustrated in Fig. 5: (1) the slope of the engineering stress $G_i = d\sigma_s/d\gamma$ at $\gamma = 0$, (2) the ultimate strength $\sigma_m = \sigma_s(\gamma_m)$, (3) the strain γ_m at ultimate strength, (4) the failure strain γ_f at which $\sigma_s(\gamma_f) = 0$, and (5) the slope of the engineering stress $G_f = d\sigma_s/d\gamma$ at γ_f. The following five equations:

$$\frac{d\sigma_s(0)}{d\gamma} - G_i = 0, \tag{13a}$$

$$\sigma_s(\gamma_m) - \sigma_m = 0, \tag{13b}$$

$$\frac{d\sigma_s(\gamma_m)}{d\gamma} = 0, \tag{13c}$$

$$\sigma_s(\gamma_f) = 0, \tag{13d}$$

$$\frac{d\sigma_s(\gamma_f)}{d\gamma} - G_f = 0, \tag{13e}$$

can be used to express the parameters in the spring network model, N_0, $N_n(\delta\gamma)$, $dN_n/d\gamma$, α, and β, in terms of the shape features of $\sigma_s(\gamma)$, i.e., G_i, σ_m, γ_m, γ_f, and G_f. We then use a Levenberg-Marquardt nonlinear least squares algorithm to find the optimal values of G_i, σ_m, γ_m, γ_f, and G_f such that $\sigma_s(\gamma)$ matches $\sigma(\gamma)$ from the athermal, quasistatic tension simulations, as well as from uniaxial tension tests of Zr-based metallic glasses in experiments.
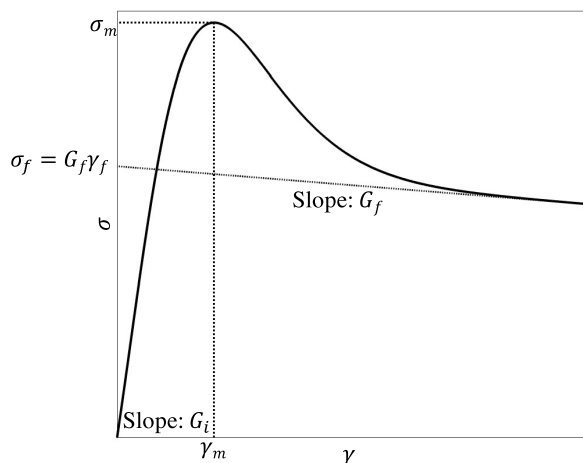
FIG. 5. Schematic of the engineering stress σ versus strain γ during uniaxial tension, including the definitions of the five parameters that characterize the shape of $\sigma(\gamma)$. G_i is the slope of $\sigma(\gamma)$ at $\gamma = 0$, σ_m is the maximum engineering stress, γ_m is the strain at which the maximum engineering stress occurs, $\sigma(\gamma_m) = \sigma_m$, $\gamma_f > 0$ is the failure strain at which $\sigma = 0$, and G_f is the slope of $\sigma(\gamma)$ at $\gamma = \gamma_f$.

III. RESULTS

In this section, we first describe the results from athermal, quasistatic simulations of the mechanical response of the LJ and EAM models of $Cu_{50}Zr_{50}$ metallic glasses to uniaxial tension. We also show the correlation between the maximum engineering stress during uniaxial tension and the potential energy per atom of the undeformed samples. We then compare the simulation results for $\sigma(\gamma)$ from athermal, quasistatic uniaxial tension to the prediction of the engineering stress versus strain from the spring network model. We show the dependence of the five parameters of the spring network model on the sample preparation protocol and relate these

parameters to key features of the shape of $\sigma(\gamma)$. Lastly, we show best fits of the spring network model to the results of experiments on uniaxial tension applied to several Zr-based metallic glasses, including $Zr_{65}Al_{10}Ni_{10}Cu_{15}$, $Cu_{49}Zr_{51}$, and $Zr_{56}Ni_{22}Al_{22}$.

A. Engineering stress versus strain from athermal, quasistatic uniaxial tension

In Fig. 6, we show $\sigma(\gamma)$ for the LJ and EAM models of $Cu_{50}Zr_{50}$ metallic glass samples obtained from thermal quenches over a range of cooling rates, instantaneous thermal quenches, and disordered FCC structures. The LJ and EAM models show qualitatively similar mechanical response over the full range of strain. For all systems, at small strains, the engineering stress increases approximately linearly with strain. The slope $d\sigma/d\gamma = G_i$ at $\gamma = 0$ is only weakly dependent on the preparation protocol of the metallic glasses. At larger strains, $\sigma(\gamma)$ becomes nonlinear and reaches a peak engineering stress σ_m that grows monotonically with decreasing cooling rate, i.e., σ_m is smallest for samples generated via instantaneous thermal quenches and is the largest for samples generated via the slowest cooling rates.

The disordered FCC structures possess the smallest σ_m of the systems in Fig. 6 and the strain at which the peak stress occurs is shifted to larger strains $\gamma_m \sim 0.2$ compared to the peak strains for the thermally quenched systems. At first, these results may seem counterintuitive. For example, it is well-known that many crystalline structures possess large peak stress at small strains and can be brittle with a rapid decrease in stress near failure. However, as shown in Fig. 16 in Appendix D, the disordered FCC structures have the largest Q_6 values, yet they are the most ductile of the systems we considered.

To illustrate why disordered FCC structures have a ductile-like response, we show a scatter plot of σ_m during uniaxial tension versus the total potential energy per atom U_0 and
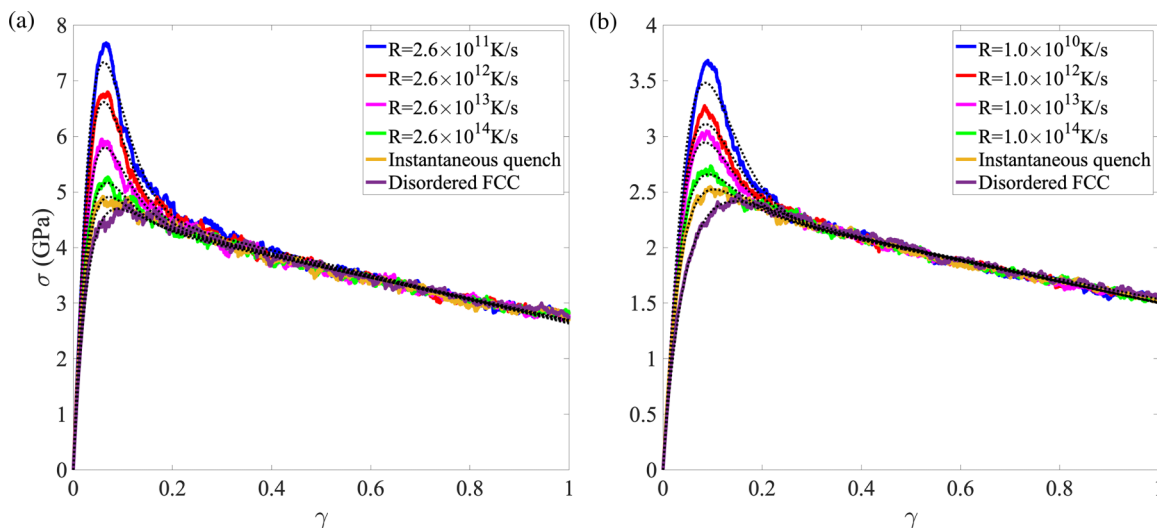

FIG. 6. Engineering stress σ plotted as a function of strain γ during uniaxial tension deformation of $Cu_{50}Zr_{50}$ metallic glass samples (solid lines) obtained using the (a) LJ and (b) EAM models for several cooling rates, the instantaneous thermal quenches, and the disordered FCC structures averaged over 50 samples. The dotted lines represent best fits of $\sigma(\gamma)$ to the prediction from the spring network model [Eq. (12)] using the parameters in Fig. 9.
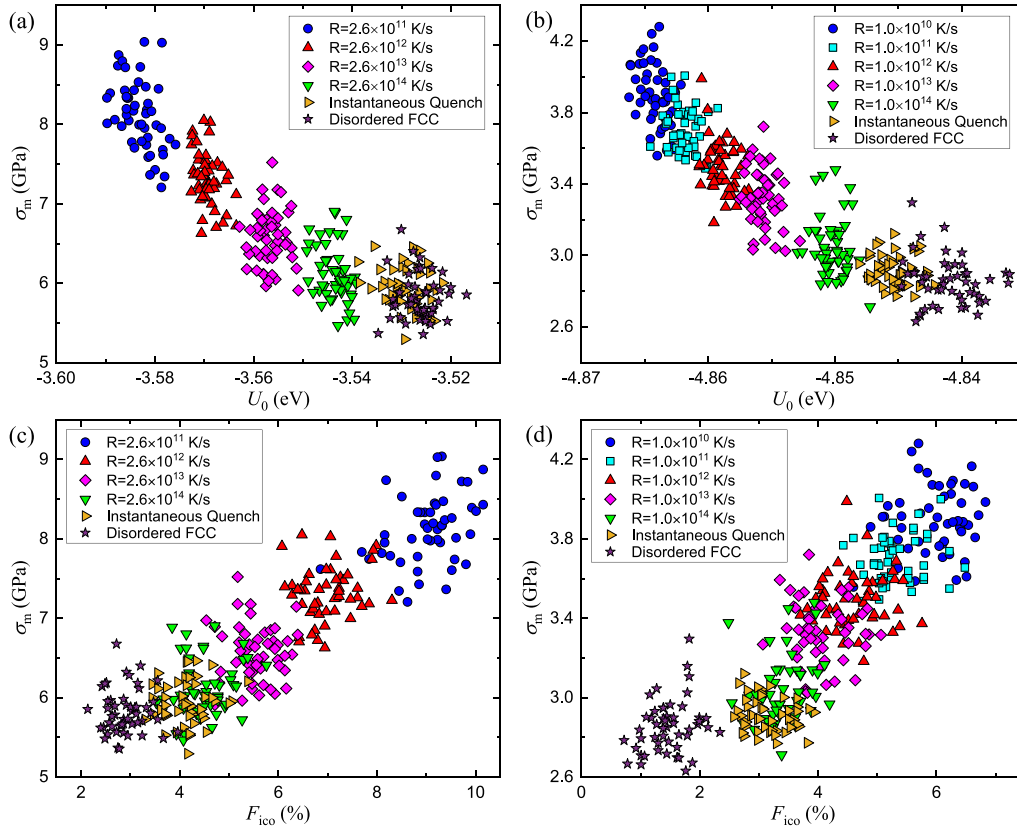
FIG. 7. Maximum engineering stress σ_m during athermal, quasistatic uniaxial tension tests plotted vs the total potential energy per atom U_0 at $\gamma = 0$ for 50 $Cu_{50}Zr_{50}$ metallic glass samples modeled using the (a) LJ and (b) EAM potentials. In addition, we plot the same data for σ_m in (a) and (b) vs the fraction of icosahedra F_{ico} based on Voronoi tessellation of the undeformed structure for the (c) LJ and (d) EAM potentials. The rightward triangles and stars represent instantaneous thermal quenches and disordered FCC structures and the other symbols represent different cooling rates R used to prepare the samples.

versus the fraction of local icosahedral structures F_{ico} of the corresponding undeformed samples in Fig. 7. (The definition of F_{ico} is provided in Appendix D.) For both the LJ and EAM models, σ_m decreases with increasing U_0 and decreasing F_{ico} on average. In particular, we find that the disordered FCC structures possess the highest U_0 and the smallest F_{ico} and σ_m values. The results for the thermally quenched systems are consistent with prior results on metallic glasses. In particular, numerous studies have found that the fictive temperature and average potential energy per atom decrease with decreasing cooling rate [64], while the fraction of icosahedra increases with decreasing cooling rate [25,65], and that increasing the fictive temperature increases the ductility of metallic glasses [11,66,67]. In the current studies, we have shown that the disordered FCC structures possess higher fictive temperatures (or U_0) than the samples that were prepared via instantaneous thermal quenches. Another important feature of $\sigma(\gamma)$ for both the LJ and EAM models of $Cu_{50}Zr_{50}$ is that it decreases roughly linearly with strain at large strains with slope $|G_f| < G_i$. Further, $\sigma(\gamma)$ is independent of the preparation protocol at large strains.

B. Comparisons to prediction of spring network model

Fits of the predictions of the spring network model to the stress versus strain curves from simulations and ex-

periments involve five parameters: kl_0N_0/A_0, $kl_0N_n(\delta\gamma)/A_0$, $kl_0(dN_n/d\gamma)/A_0$, α, and β. However, kl_0N_0/A_0 is set to the slope of $\sigma(\gamma)$ at $\gamma = 0$ and remains constant during the fitting procedure. The shape parameter α for the Gamma distribution of cutoff strains $P(\gamma_c)$ is initially set to 1, assuming that only one spring breaks at a time during the tensile test, and the initial value of the rate parameter β for $P(\gamma_c)$ is set to α/γ_m. In Fig. 6, we show the best fits of σ_s for the spring network model to $\sigma(\gamma)$ from the simulations of athermal, quasistatic uniaxial tension for the LJ and EAM models of $Cu_{50}Zr_{50}$ for all sample preparation protocols. In general, different initial values of these parameters give rise to very similar fitting parameters and the fits are high quality for both the LJ and EAM models for all preparation protocols. The only discrepancy occurs for the slowest cooled samples, where the fit slightly underestimates σ_m. [This small discrepancy can be removed by generalizing the distribution of strain cutoffs $P(\gamma_c)$ to include an additional shape parameter.] To assess the quality of the fits of the predicted $\sigma_s(\gamma)$ for the spring network model to $\sigma(\gamma)$ from the atomistic simulations, we calculate the root-mean-square error,

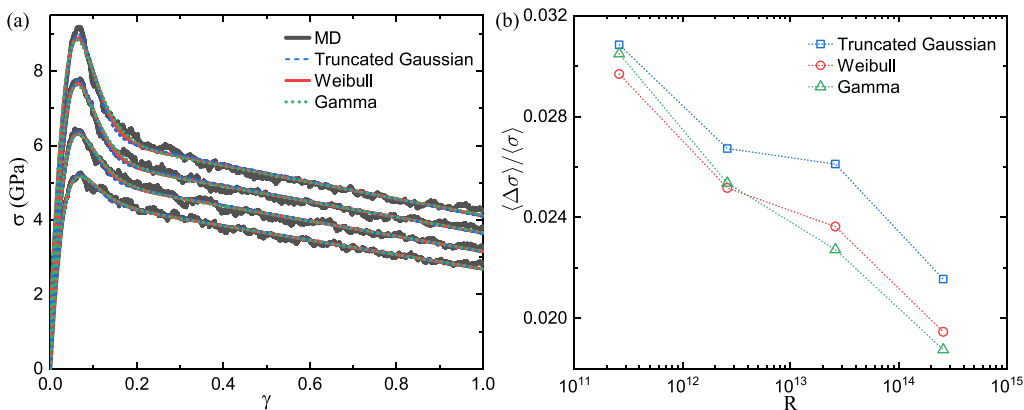$$\langle\Delta\sigma\rangle = \sqrt{\frac{\sum_{i=1}^{n}(\sigma(\gamma_i) - \sigma_s(\gamma_i))^2}{n}}, \quad (14)$$

FIG. 8. (a) Engineering stress σ plotted as a function of strain γ for athermal, quasistatic simulations of uniaxial tension on LJ models of $Cu_{50}Zr_{50}$ metallic glasses obtained from four cooling rates, $R = 2.6 \times 10^{11}$, 2.6×10^{12}, 2.6×10^{13}, and 2.6×10^{14} K/s (with decreasing σ_m). From the slowest to fastest cooling rates, the $\sigma(\gamma)$ curves are vertically shifted by 1.5, 1, 0.5, and 0 GPa. We also show fits of $\sigma(\gamma)$ to the predictions of the spring network model using different distributions $P(\gamma_c)$ of cutoff strains. (b) Normalized root-mean-square error $\langle \Delta\sigma \rangle / \langle \sigma \rangle$ between the simulation data and spring network predictions for the engineering stress plotted as a function of the cooling rate R used to prepare the metallic glass samples, as well as different forms for $P(\gamma_c)$.
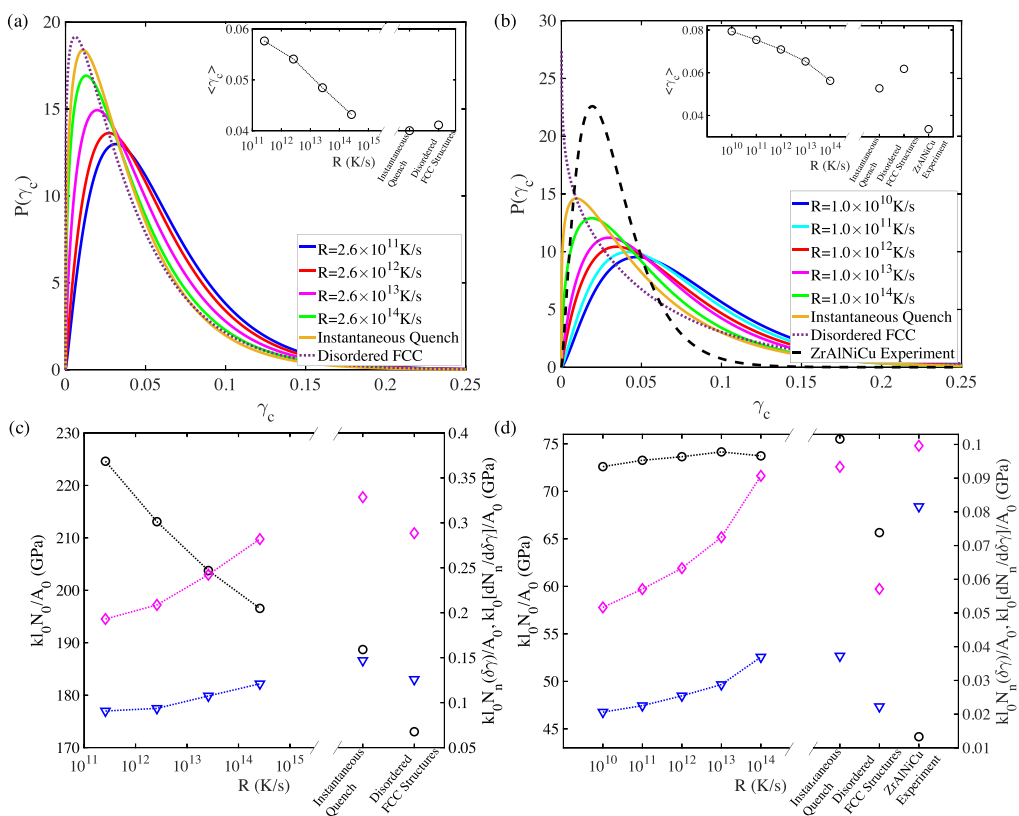

FIG. 9. The optimal values of the parameters of the spring network model obtained from best fits of $\sigma_s(\gamma)$ to $\sigma(\gamma)$ from the athermal, quasistatic uniaxial tension simulations of the LJ [(a), (c)] and EAM [(b), (d)] models of $Cu_{50}Zr_{50}$. Panels (b) and (d) also show optimal values of the parameters for $\sigma(\gamma)$ obtained from experimental studies of uniaxial tension on $Zr_{65}Al_{10}Ni_{10}Cu_{15}$ metallic glasses performed at 593 K [10]. $\sigma(\gamma)$ from these experiments is shown in Fig. 12(a). Panels (a) and (b) and their insets show the variation of $P(\gamma_c)$ and the average $\langle \gamma_c \rangle$ with the sample preparation protocols and experimental studies. In the main panels (a) and (b), the thermal quenches, disordered FCC samples, and experimental studies are represented by solid, dotted, and dashed lines, respectively. Panels (c) and (d) show $kl_0 N_0 / A_0$ (circles) on the left vertical axis, and $kl_0 N_n(0) / A_0$ (diamonds) and $kl_0 (dN_n / d\gamma) / A_0$ (triangles) on the right vertical axis for the different sample preparation protocols and experimental studies.

where $\gamma_i = i\delta\gamma$ and $n = 1/\delta\gamma$. We find that the normalized root-mean-square error $\langle\Delta\sigma\rangle/\langle\sigma\rangle \lesssim 0.03$ for all of the simulations of athermal, quasistatic uniaxial tension that we performed. We also fit the numerical simulations of stress versus strain to the predictions of the spring network model using the truncated Gaussian and Weibull distributions for $P(\gamma_c)$. Using these cutoff strain distributions, the spring network model can recapitulate the stress versus strain behavior of metallic glasses undergoing uniaxial tensile loading with similar accuracy to that using Gamma distribution for $P(\gamma_c)$ (with $\langle\Delta\sigma\rangle/\langle\sigma\rangle \lesssim 0.03$), as shown in Fig. 8. Thus, one advantage of the spring network model is that its parameters can be obtained from a single stress versus strain curve and it can qualitatively recapitulate the stress versus strain behavior of metallic glasses undergoing uniaxial tension without sensitivity to the particular form of the cutoff strain distribution.

The spring network parameters obtained from the fits are displayed in Fig. 9. In panels (a) and (b), we show how the cutoff distribution $P(\gamma_c)$ and its average $\langle\gamma_c\rangle$ vary with the sample preparation protocol for the LJ and EAM models of $Cu_{50}Zr_{50}$. The results are similar for the LJ and EAM models. $P(\gamma_c)$ shifts to larger strains and becomes broader as the cooling rate is *decreased*. The shift and broadening of the distribution toward larger strains indicate that the springs can withstand more elongation before breaking when the sample is prepared at lower cooling rates. These results are consistent with previous simulation studies [68] of shear stress versus strain during athermal, quasistatic simple shear of model metallic glasses. They showed that the frequency of atomic rearrangements and energy loss per rearrangement are reduced for slowly cooled glasses at small strains. For the disordered FCC structures, $P(\gamma_c)$ is shifted to low values of strain, which indicates that the springs begin to break immediately after the application of uniaxial tension in these samples.

In Figs. 9(c) and 9(d), we show kl_0N_0/A_0, $kl_0N_n(0)/A_0$, and $kl_0(dN_n/d\gamma)/A_0$ for metallic glass samples with different preparation protocols. For the LJ model, kl_0N_0/A_0 decreases with increasing cooling rate, whereas kl_0N_0/A_0 is weakly dependent on cooling rate for the EAM model, with a slight decrease for the FCC disordered structures. For both LJ and EAM models of $Cu_{50}Zr_{50}$, more rapidly cooled glasses possess larger values of $kl_0N_n(0)/A$ and $kl_0(dN_n/d\gamma)/A$. Thus, more new springs are generated for more rapidly cooled glasses. However, since the cutoff distribution $P(\gamma_c)$ is shifted to smaller strains for more rapidly cooled glasses, these new springs break more frequently. LJ disordered FCC structures possess values of $kl_0N_n(0)/A$ and $kl_0(dN_n/d\gamma)/A_0$ that are comparable to the most rapidly cooled metallic glasses, which is consistent with the fact that they have small σ_m. Instead, $kl_0N_n(0)/A_0$ and $kl_0(dN_n/d\gamma)/A_0$ for the EAM disordered FCC structures are comparable to the values for slowly cooled glasses.

The predicted stress from the spring network model, $\sigma_s(\gamma) = \sigma_{s0}(\gamma) + \sigma_{sn}(\gamma)$, can be decomposed into contributions from the initial springs σ_{s0} that were present at $\gamma = 0$ and from the new springs σ_{sn} that continue forming after the initial springs break (see Fig. 10). We find that the stress contribution from the initial springs, which is controlled by the initial number of springs and the cutoff distribution $P(\gamma_c)$, is strongly protocol dependent. Further, the contribution from
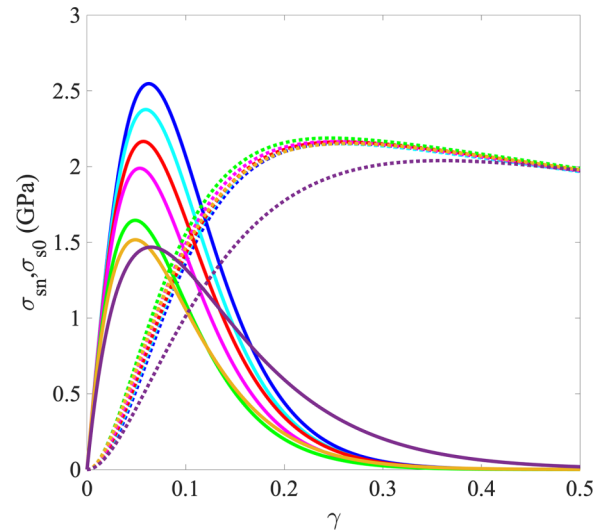

FIG. 10. $\sigma_s(\gamma)$ from the spring network model [Eq. (11)] can be decomposed into contributions from the initial springs σ_{s0} (solid lines) and new springs σ_{sn} (dotted lines). We show results from best fits to the EAM model for $Cu_{50}Zr_{50}$ samples generated using cooling rates $R = 10^{10}$ K/s (blue), 10^{11} K/s (cyan), 10^{12} K/s (red), 10^{13} K/s (magenta), and 10^{14} K/s (green), instantaneous quenches (yellow), and disordered FCC structures (purple).

the initial springs is large at small strains and decays to zero at large strains. In contrast, σ_{sn} is zero at small strains and $\sigma_{sn} \gg \sigma_{s0}$ at large strains. For all thermally quenched samples and for the disordered FCC structures at sufficiently large strains, the stress contribution from the new springs $\sigma_{sn} \sim \sigma_s$ is independent of the sample preparation protocol. This result implies that the variation of $P(\gamma_c)$ with the preparation protocol [cf. Figs. 9(a) and 9(b)] exactly offsets the variation of $kl_0N_n(0)/A_0$ and $kl_0(dN_n/d\gamma)/A_0$ with the preparation protocol [cf. Figs. 9(c) and 9(d)].

As described in Sec. II E, we can understand key features of the engineering stress versus strain curves from the parameters in the spring network model. As an example, in Fig. 11, we show the peak stress σ_m and the strain γ_m at which it occurs as determined directly from the five optimal spring network parameters obtained from fits of $\sigma_s(\gamma)$ to $\sigma(\gamma)$. As we found previously in Fig. 6, σ_m decreases with increasing cooling rate and the disordered FCC structures possess the smallest σ_m. γ_m increases weakly with increasing cooling rate and is the largest for the disordered FCC structures. These results illustrate the high-quality fits of the spring network model and emphasize that we can in principle determine the macroscopic stress versus strain relation by determining the *local* structural and mechanical properties of metallic glasses.

In Fig. 12, we compare the predictions of $\sigma_s(\gamma)$ from the spring network model to the engineering stress versus strain from experimental studies of uniaxial tensile deformations of $Zr_{65}Al_{10}Ni_{10}Cu_{15}$, $Cu_{49}Zr_{51}$, and $Zr_{56}Ni_{22}Al_{22}$ metallic glass samples [3,6,10]. In Fig. 12(a), we show $\sigma(\gamma)$ obtained from deforming $Zr_{65}Al_{10}Ni_{10}Cu_{15}$ samples with cross-sectional area 0.02 mm^2 at strain rate $\dot{\gamma} = 5 \times 10^{-4}$ s^{-1} and tested at temperatures $T = 593$ K, 613 K, and 633 K [10]. These prior

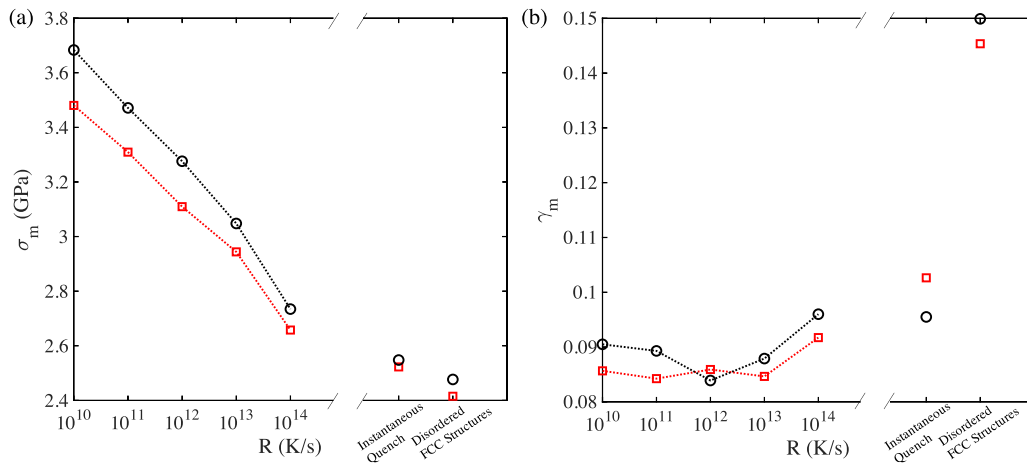FIG. 11. (a) Maximum engineering stress σ_m and (b) the strain γ_m at which $\sigma(\gamma_m) = \sigma_m$ calculated directly from the spring network parameters [Eq. (13)] obtained from best fits of the data from the simulations of athermal, quasistatic uniaxial tension of $Cu_{50}Zr_{50}$ modeled using the EAM model (red squares). The black circles indicate results directly from $\sigma(\gamma)$ obtained from simulations of athermal, quasistatic uniaxial tensile deformations.

experimental studies find that $\sigma(\gamma)$ for the $Zr_{65}Al_{10}Ni_{10}Cu_{15}$ samples possess large-strain tails prior to fracture for $T > 513$ K (cf. Fig. 6). $\sigma_s(\gamma)$ from the spring network model can fit $\sigma(\gamma)$ for $Zr_{65}Al_{10}Ni_{10}Cu_{15}$ with normalized root-mean-square error values $\langle \Delta\sigma \rangle / \langle \sigma \rangle \lesssim 0.04$. In Figs. 9(b) and 9(d), we show the optimal parameters for the spring network model obtained from best fits of $\sigma_s(\gamma)$ to $\sigma(\gamma)$ from the $Zr_{65}Al_{10}Ni_{10}Cu_{15}$ sample strained at $T = 593$ K. The best-fit spring network parameters for the experimental results are of the same order of magnitude as those obtained from best fits to the athermal, quasistatic uniaxial tension simulations of $Cu_{50}Zr_{50}$ modeled using the LJ and EAM models. (Note that EAM potentials are not publicly available for ZrAlNiCu and ZrNiAl alloys [69–71].) These results suggest that the spring network model can be used to describe the mechanical response of metallic glasses at finite temperatures and strained at nonzero strain rates.

Figure 12(b) features $\sigma(\gamma)$ obtained from uniaxial tensile deformation of $Cu_{49}Zr_{51}$ and $Zr_{56}Ni_{22}Al_{22}$ metallic glass samples. The $Cu_{49}Zr_{51}$ sample has a diameter of 80 nm and is pulled at strain rate $\dot{\gamma} \sim 10^{-3}$ s^{-1} at room temperature [6]. We also considered two sputtered $Zr_{56}Ni_{22}Al_{22}$ samples that have thickness $\sim$90 nm and are also strained at $\dot{\gamma} \sim 10^{-3}$ s^{-1} at room temperature [3]. (As-sputtered samples experience cooling rates in the range $10^8 - 10^{10}$ K/s [72–74].) One of the two sputtered samples was annealed at sub-T_g temperatures. (ZrNiAl alloys have been found to be good glass formers due to the addition of Al [75,76].) The metallic glass samples strained at room temperature do not exhibit large-strain tails in $\sigma(\gamma)$, and instead the samples fracture at small strains $\gamma \sim 0.1$. As a result, the optimal values for the number and rate of change of new springs with strain, $k l_0 N_n(0)/A_0$ and $k l_0 (dN_n/d\gamma)/A_0$, are close to zero, and the number of initial springs and distribution of spring breaking cutoffs $P(\gamma_c)$
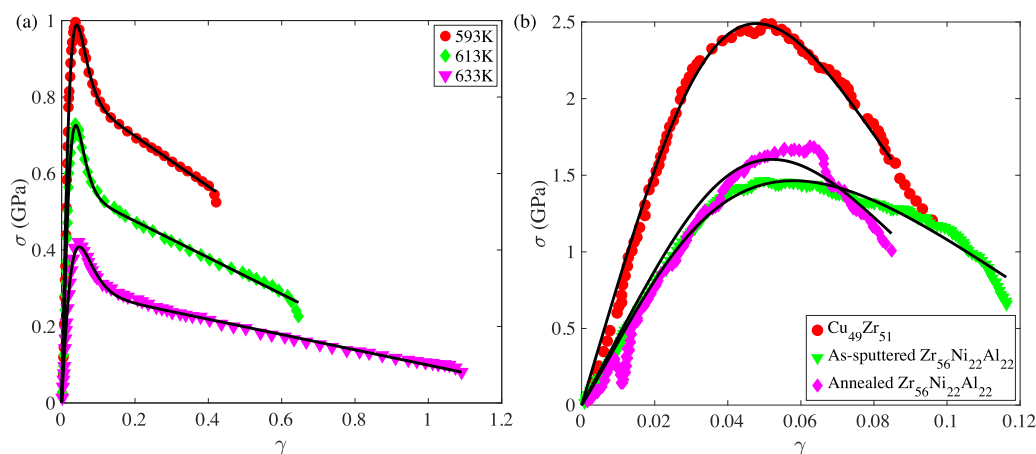

FIG. 12. Engineering stress σ vs strain γ from experimental studies of uniaxial tensile deformations applied to several metallic glasses: (a) $Zr_{65}Al_{10}Ni_{10}Cu_{15}$ samples tested at 593 K (red circles), 613 K (green diamonds), and 633 K (magenta triangles) [10] and (b) a nm-scale $Cu_{49}Zr_{51}$ [6] sample (red circles) and two sputtered $Zr_{56}Ni_{22}Al_{22}$ [3] samples. The $Zr_{56}Ni_{22}Al_{22}$ samples were as sputtered (green diamonds) and annealed below T_g (magenta triangles). The black solid lines are best fits to $\sigma_s(\gamma)$ [Eq. (12)] from the spring network model.

mainly determine $\sigma(\gamma)$. Even in this case, the best fits of $\sigma_s(\gamma)$ from the spring network model to $\sigma(\gamma)$ from the experiments give normalized root-mean-square error (rms) values $\langle \Delta \sigma \rangle / \langle \sigma \rangle \lesssim 0.1$.

These experimental studies of tensile loading of metallic glasses were carried out on much larger samples over a range of finite temperatures, $0.4 \leqslant T/T_g \leqslant 0.97$, compared to the numerical simulations. The zero-temperature tensile loading in the simulations and finite-temperature, nonzero strain rate tensile loading in the experiments explore different sets of physical conditions, providing independent sets of stress versus strain curves. The fact that the spring network model can accurately recapitulate the different stress versus strain curves in both cases is another important advantage of the spring network model.

IV. CONCLUSIONS AND FUTURE DIRECTIONS

In this article, we developed a coarse-grained spring network model to describe the mechanical response of metallic glasses to uniaxial tension. We first performed athermal, quasistatic uniaxial tension simulations of $Cu_{50}Zr_{50}$ metallic glasses modeled using both the Lennard-Jones and EAM potentials. From these simulations, we calculated the engineering stress versus strain $\sigma(\gamma)$ from samples generated over a wide range of cooling rates and different amounts of local positional order. In general, $\sigma(\gamma)$ had the same qualitative form for both the LJ and EAM simulations. We found that the peak σ_m in the engineering stress versus strain decreases as the total potential energy per atom of the undeformed structure increases, which shows that one can predict key features of $\sigma(\gamma)$ without actually performing the tensile tests. Further, we showed that the disordered FCC structures possess more ductile mechanical response than the rapidly cooled metallic glass samples. We analytically solved the one-dimensional spring network model for the total force exerted by the springs as a function of strain. In the spring network model, initial springs present at $\gamma = 0$ stretch during the applied strain and break when they exceed cutoff strains γ_c that are selected from a Gamma distribution $P(\gamma_c)$. However, the predictions of the spring network model are not extremely sensitive to the form of this distribution. In addition, new springs can form, and then stretch and break in the same way as the initial springs.

The engineering stress $\sigma_s(\gamma)$ predicted from the spring network model includes five parameters. Two of the parameters define the shape of the cutoff strain distribution $P(\gamma_c)$. The three other parameters are related to the number of initial springs, and the number of new springs and rate of change of the number of new springs with strain. We showed that we can express these five parameters in terms of important features of the shape of $\sigma(\gamma)$, i.e., the slope $d\sigma/d\gamma$ at $\gamma = 0$, maximum stress σ_m, strain γ_m at which the maximum stress occurs, strain γ_f at fracture (i.e. $\sigma = 0$ at large strains), and slope $d\sigma/d\gamma$ at γ_f. After fitting the spring network model to $\sigma(\gamma)$ from the simulations, we found that the cutoff strain distribution shifts to larger strains for more slowly cooled glasses. In contrast, the number and rate of change of new springs decreases for slowly cooled glasses. These two sets of changes offset each other at large strains since $\sigma(\gamma)$ is nearly independent of the sample preparation

protocol in this regime. Lastly, we showed that the spring network model can be used to describe the results of experimental studies of uniaxial tensile tests of several Zr-based metallic glasses at temperatures above and below room temperature, where they possess large-strain tails in $\sigma(\gamma)$ and where they fracture at small strains, respectively. Thus, the spring network model displays versatility and generality. It can accurately describe the ensemble-averaged stress versus strain curves from numerical simulations of small samples undergoing athermal, quasistatic tensile loading, as well as the smooth stress versus strain curves from experimental studies of tensile loading at elevated temperatures and finite strain rates.

There are several promising directions for future work. First, we will focus on extracting the spring model parameters from the atomistic simulations of uniaxial tension. For example, we can estimate the number of initial springs by determining the distribution of the sizes of the stress drops that occur during uniaxial tension of single, finite-sized samples. To determine the shape of the cutoff strain distribution, number of new springs, and their rate of change with strain from the atomistic simulations, we can add a perturbation to the position of a single atom, minimize the total potential energy, and measure changes in nearest-neighbor atoms and the engineering stress as a function of the size of the perturbation. Thus, using the spring network model, we can link bulk mechanical properties to atomistic structure and interactions in metallic glasses. Second, we will generalize the spring network model so that it can describe the mechanical response of metallic glasses under simple and pure shear deformations, for example, by using several sets of parallel springs that connect the corners of the simulation box (see Fig. 13). Third, when a finite number of springs is used, as shown in Fig. 20(a) in Appendix E with $N_s = 256$ springs, the predictions of the spring network model can describe serrated stress versus strain curves, which occur in small metallic glass samples, low temperatures, and slow strain rates, and have been observed in numerous experimental studies [47–49]. Although the distributions of stress drops from the predictions of the spring network model and MD simulations of $Cu_{50}Zr_{50}$ are qualitatively similar, i.e., the frequency of stress drops decreases rapidly with the size of the drop as shown in Fig. 20(b), the current spring network model generates more small stress drops and less large ones than the MD simulations. Further studies of the spring network model are required to quantitatively reproduce the distribution of stress drops from MD simulations of metallic glasses under uniaxial loads. Fourth, in the current paper, we focused on systems that do not form large-scale shear bands. In future work, we will consider systems prepared using hybrid Monte Carlo and molecular dynamics methods that can reach cooling rates lower than 10^6 K/s [25] and increase the aspect ratio of the sample to obtain strong shear banding behavior as shown in Appendix C. We will couple springs with different distributions of breaking strains in parallel and series to model shear banding and fracture behaviors, where cascades of weak springs can break at the same time and cause large stress drops and large-scale, collective atomic motion [77] (see Fig. 13). Finally, we will conduct molecular dynamics simulations of $Cu_{50}Zr_{50}$ at finite temperatures to study the mechanical response of metallic
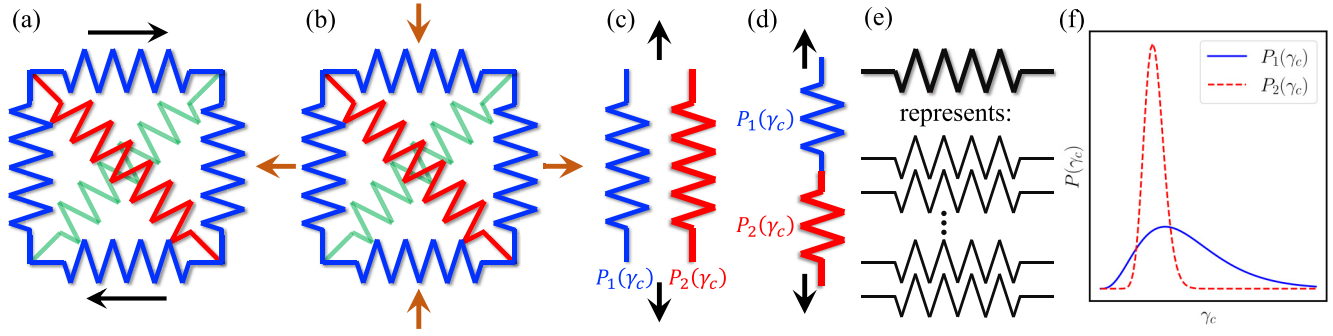
FIG. 13. Generalizations of the spring network model that can describe (a) simple and (b) pure shear loading geometries; (c) shear-banding instabilities in the mechanical response; and (d) fracture of metallic glasses. Each spring in (a)–(d) represents a set of parallel springs with no actual physical separation in the transverse direction to the line connecting the spring endpoints, as depicted in (e). The sets of red, green, and blue parallel springs in (a) and (b) are uncoupled. The two sets of springs in (c) and (d) follow distinct distributions of breaking strain $P(\gamma_c)$, as shown in (f). Red springs, which are fewer in number, exhibit a much narrower distribution of γ_c, such that a significant number of red springs can break at the same γ_c, which gives rise to shear banding and fracture behaviors.

glasses to tensile loading at nonzero temperatures and strain rates, so that we can systematically determine the variation of the spring network parameters with temperature and strain rate below T_g.

APPENDIX A: ATOMIC INTERACTION POTENTIALS FOR Cu$_{50}$Zr$_{50}$

We consider the LJ [24] and EAM interaction potentials [78] for modeling Cu$_{50}$Zr$_{50}$ metallic glasses. The LJ potential includes isotropic, pairwise atomic interactions with parameters that control the atomic size and the attractive strength of the interactions.

For the systems with LJ interactions, we employ a truncated and force-shifted potential energy,

$$U_{ij}(r_{ij}) = \phi(r_{ij}) - \phi(r_c) - (r_{ij} - r_c)\frac{d\phi_{ij}}{dr_{ij}}\bigg|_{r_{ij}=r_c} \quad \text{(A1)}$$

for $r_{ij} < r_c$ and $U_{ij}(r_{ij}) = 0$ for $r_{ij} \geqslant r_c$, where r_{ij} is the separation between atoms i and j, $r_c = 2.5\sigma_{ij}$, and

$$\phi_{ij}(r_{ij}) = 4\epsilon_{ij}[(\sigma_{ij}/r_{ij})^{12} - (\sigma_{ij}/r_{ij})^6]. \quad \text{(A2)}$$

The total potential energy is the sum of $U_{ij}(r_{ij})$ over distinct atomic pairs, $U = \sum_{i>j} U_{ij}(r_{ij})$ and the pair force on atom i from j is $\vec{F}_{ij} = -(dU/dr_{ij})\hat{r}_{ij}$, where $\hat{r}_{ij}$ is the unit vector that points from the center of atom i to the center of j.

We assume that A-type atoms are Zr and B-type atoms are Cu. We set the the energy and length parameters in Eq. (A2) as follows: $\sigma_{BB}/\sigma_{AA} = 0.7975$, $\sigma_{AB}/\sigma_{AA} = (1 + \sigma_{BB}/\sigma_{AA})/2$, $\epsilon_{BB}/\epsilon_{AA} = 0.5584$, and $\epsilon_{AB}/\epsilon_{AA} = (1 + \epsilon_{BB}/\epsilon_{AA})/2 - \Delta H_{mix}/\epsilon_{AA} = 0.8167$ using experimental

values of the atomic radii [79], cohesive energy [80], and heat of mixing [81]. The mass ratio is set to $m_A/m_B = 1.435$, which is the ratio of the molar masses of Zr and Cu.

When we describe the LJ simulation results, we convert length and energy scales into physical units using $\sigma_{AA} = 2.9$ Å and $\epsilon_{AA} = 0.74$ eV [82]. For these values, Zr atoms on an HCP lattice yield a cohesive energy of 6.47 eV and lattice constant of 3.22 Å, which match experimental results [78]. The temperature, pressure, and time scales are then $\epsilon_{AA}/k_B = 8.6 \times 10^3$ K, $\epsilon_{AA}/\sigma_{AA}^3 = 4.7$ GPa, and $\sigma_{AA}\sqrt{m_{AA}/\epsilon_{AA}} = 0.33$ ps, where k_B is Boltzmann's constant.

EAM potentials include both pairwise atomic interactions, as well as many-body interactions that arise from the electronic degrees of freedom. We considered an EAM interaction potential to model the mechanical response of Cu$_{50}$Zr$_{50}$ to uniaxial tension. We selected the EAM potential developed by Mendelev et al., who studied vitrification of CuZr alloys [78]. For the EAM, the total potential energy is the sum of two terms [83],

$$U = \sum_{i=1}^{N} \mathcal{F}_\lambda \left(\sum_{j \neq i} \rho_\mu(r_{ij}) \right) + \sum_{i>j} \phi_{\lambda\mu}^p(r_{ij}), \quad \text{(A3)}$$

where $\mathcal{F}_\lambda$ is the many-body embedding function that depends on the electron density ρ_μ, $\phi_{\lambda\mu}^p$ is the pairwise interaction term and λ, μ are the element types of atoms i and j. Both the many-body and pairwise terms have a cutoff of $r_c = 7.6$ Å beyond which $U = 0$. This EAM potential was calibrated to match the formation energies of the CuZr equilibrium crystal phases at zero temperature, and the atomic density, mixing enthalpy, and partial-pair correlation functions at 1000K for Cu$_{46}$Zr$_{54}$. In addition, Zhang et al. [25] used this EAM potential to prepare amorphous Cu$_{50}$Zr$_{50}$ samples using a hybrid Monte Carlo (MC) and molecular dynamics (MD) simulation technique at effective cooling rates as low as 500 K/s. The structure factor and shear modulus of the slow quenched Cu$_{50}$Zr$_{50}$ samples obtained from the hybrid MC/MD technique were similar to those obtained
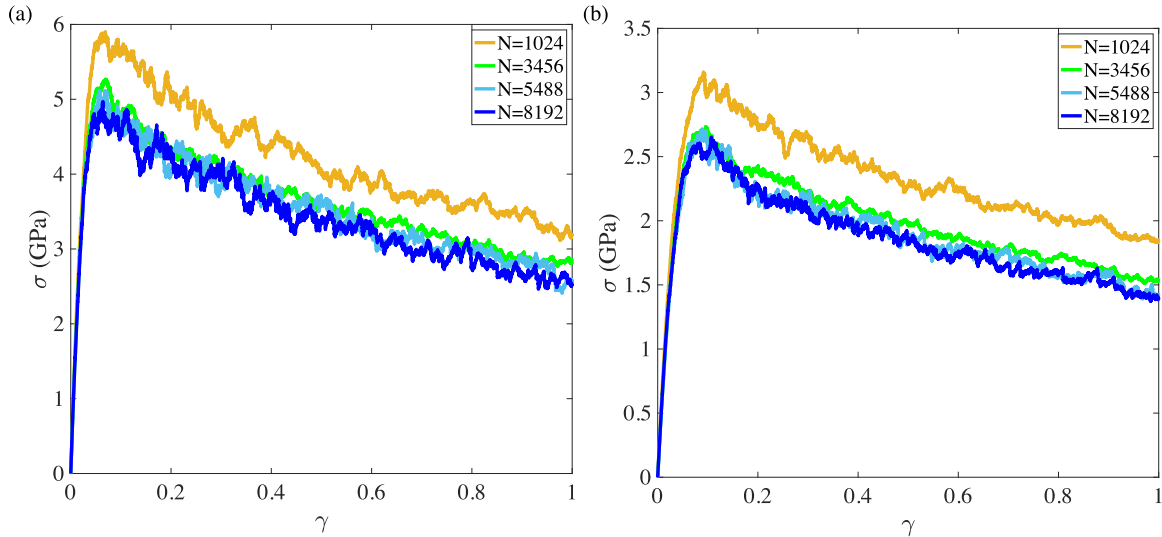
FIG. 14. Engineering stress σ plotted as a function of strain γ for athermal, quasistatic simulations of $Cu_{50}Zr_{50}$ (modeled using (a) LJ and (b) EAM interactions) undergoing uniaxial strain for system sizes $N = 1024$, 3456, 5488, and 8192. The systems with LJ and EAM interactions were cooled at rates R = 2.6×10^{14} K/s and 1.0×10^{14} K/s, respectively. The engineering stress was averaged over 50 configurations for $N = 1024$ and 3456 and over 10 configurations for the other system sizes.

experimentally at comparable cooling rates. We also measured the melting temperature T_m of pure Zr and pure Cu with this EAM potential using the method described by Tang and Harrowell [84]. We found $T_m \sim 2110$ K for Zr and ~ 1356 K for Cu for this EAM potential, which are similar to the experimental values of $T_m \sim 2128$ K and ~ 1358 K for Zr and Cu, respectively.

APPENDIX B: SYSTEM-SIZE EFFECTS ON ENGINEERING STRESS VERSUS STRAIN

In this Appendix, we investigate the dependence of the engineering stress versus strain on system size for the athermal, quasistatic simulations of uniaxial strain. In Fig. 14, we show σ versus γ for $Cu_{50}Zr_{50}$ metallic glass samples modeled using (a) LJ and (b) EAM interactions for several system sizes, $N = 1024$, 3456, 5488, and 8192. The systems with LJ and EAM interactions were prepared using cooling rates $R = 2.6 \times 10^{14}$ K/s and 1.0×10^{14} K/s, respectively. For systems with both LJ and EAM interactions, $\sigma(\gamma)$ for $N = 1024$ differs significantly from the other system sizes, whereas $\sigma(\gamma)$ for $N \geqslant 3456$ does not depend sensitively on system size. We observe similar behavior for the system-size dependence of $\sigma(\gamma)$ in Fig. 14 for the other cooling rates we considered in the main text. Thus, in the main text we present results for $\sigma(\gamma)$ for systems with $N = 3456$ atoms.

APPENDIX C: SHEAR BANDS

Shear bands refer to a type of plastic instability that localizes large shear strains in a relatively narrow zone of the system when it is subjected to applied deformations. Shear bands are typically accompanied by large stress drops in the material. In the current set of numerical simulations, we prepared the metallic glass samples using relatively fast cooling rates ($R \sim 10^{10} - 10^{14}$ K/s) and used samples with small

aspect ratios ($L_z/L_x = L_z/L_y = 1/2$) prior to deformation, and thus we did not observe large stress drops that indicate large-scale shear banding. In addition, we also measured the metric $D_{\min,i}^2$ that quantifies the nonaffine atomic motion for each atom i for two configurations separated by a small strain,

$$D_{\min,i}^2 = \frac{1}{n\overline{d}^2} \sum_{j=1}^{n} \|\vec{r}_{ij,a} - F\vec{r}_{ij,0}\|^2, \qquad (C1)$$

where $\overline{d}$ is the average atomic diameter of the system, n is the number of neighbors of atom i within a distance of 3.8 Å (position of the first minimum of the radial distribution function), $\vec{r}_{ij,0}$ and $\vec{r}_{ij,a}$ are the relative positions between neighboring atom j and atom i for configurations before and after the application of a small strain, and F is the best-fit deformation gradient tensor [85]. For the metallic glass samples generated via numerical simulations in the main text, we do not find large spatial correlations among atoms with $D_{\min,i}^2 > 0.04$. Therefore, the numerically generated samples in the main text do not possess large-scale shear bands. Nevertheless, we also applied athermal, quasistatic tensile deformations to $Cu_{50}Zr_{50}$ metallic glasses (using the EAM potential) with larger initial aspect ratios of $L_z/L_x = L_z/L_y = 3$ and prepared using a much lower cooling rate $R \sim 3 \times 10^6$ K/s. These elongated and lower-energy samples can possess large-scale shear bands during athermal, quasistatic tensile loading. As demonstrated in Fig. 15(a), a large stress drop $\delta\sigma \approx 1.4$ GPa is observed at strain $\gamma \sim 0.1$, which is the result of a large shear band that forms in the sample [see Fig. 15(b)]. As discussed above, the comparisons in the main text between the predictions of shear stress versus strain for the spring network model and numerical simulations do not consider large-scale shear band formation. In future work, we will couple springs with different distributions of cutoff strains in parallel and series to model shear-banding and fracture behaviors.
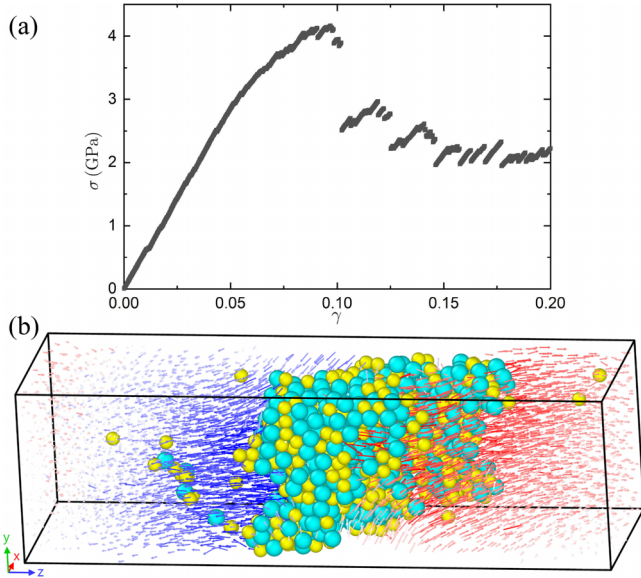
FIG. 15. (a) Engineering stress vs strain for a $Cu_{50}Zr_{50}$ sample (modeled using the EAM potential and prepared using a cooling rate $R \sim 3 \times 10^6$ K/s) obtained from athermal, quasistatic uniaxial tension in the z direction. The system contains $N = 6000$ atoms within a cuboidal box with initial aspect ratios $L_z/L_x = 3$ and $L_z/L_y = 3$ before deformation and with periodic boundary conditions in the z direction and open boundaries in the x and y directions. (b) Nonaffine displacement field (scaled by a factor of 2) obtained by comparing configurations before and after the largest stress drop near $\gamma \sim 0.1$ in (a). The vectors are colored based on whether they have positive (red) or negative (blue) z components of the nonaffine displacement field. Only atoms with $D_{\min,i}^2 > 0.04$ are shown.

APPENDIX D: LOCAL ATOMIC ENVIRONMENT

We can characterize the local degree of positional order in a given atomic configuration using the sixfold local bond orientational order (BOO) parameter Q_6, which gives the degree of sixfold orientational symmetry of that atom's nearest neighbors [86]. Typically, $Q_6 \gtrsim 0.25$ for a crystal-like atom and Q_6 takes on smaller values for atoms in icosahedral or other amorphous structural motifs [87,88]. Atoms in FCC and HCP lattices have $Q_6 = 0.575$ and 0.484, respectively.

The l-fold local BOO parameter of atom i is defined using

$$q_{lm}(i) = \frac{1}{N_i} \sum_{j=1}^{N_i} \frac{A_{ij}}{A_{tot}^i} Y_{lm}(\theta(\mathbf{r}_{ij}), \phi(\mathbf{r}_{ij})), \quad \text{(D1)}$$

where N_i is the number of Voronoi neighbors [89] of atom i, A_{ij} is the area of the Voronoi face shared by atoms i and j, A_{tot}^i is the total area of all faces belonging to the Voronoi polyhedron of atom i, $Y_{lm}(\theta(\vec{r}_{ij}), \phi(\vec{r}_{ij}))$ is the spherical harmonic function of degree l and order m, $\theta(\vec{r}_{ij})$ and $\phi(\vec{r}_{ij})$ are the polar and azimuthal angles that parametrize the orientation of the vector $\vec{r}_{ij}$ connecting atoms i and j [90]. We then average $q_{lm}(i)$ to obtain [91]

$$Q_{lm}(i) = \frac{1}{N_i + 1} \left(q_{lm}(i) + \sum_{j=1}^{N_i} q_{lm}(j) \right). \quad \text{(D2)}$$
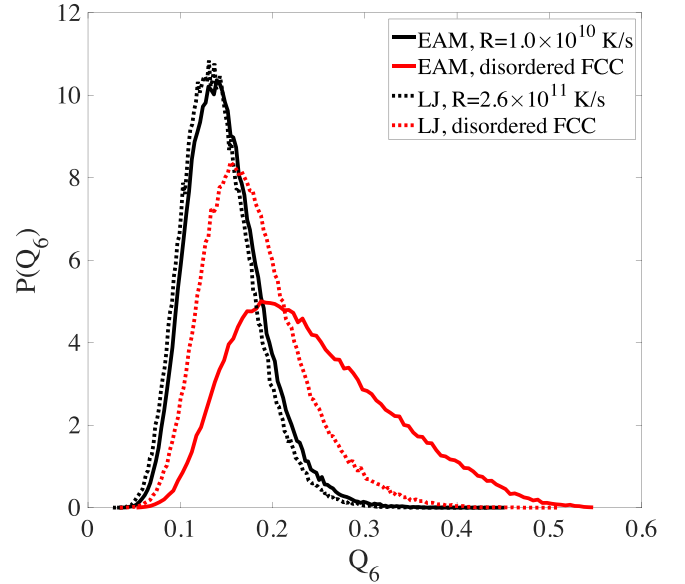

FIG. 16. Probability distribution of the local bond-orientational order parameter $P(Q_6)$ for each atom in $Cu_{50}Zr_{50}$ metallic glasses prepared by thermally quenching at cooling rates, $R = 2.6 \times 10^{11}$ K/s and 1.0×10^{10} K/s for the LJ and EAM models and in disordered FCC structures obtained by randomly placing Cu and Zr atoms on an FCC lattice followed by potential energy minimization.

The l-fold local BOO parameter Q_l is then defined by averaging over the m values associated with a given l,

$$Q_l(i) = \sqrt{\frac{4\pi}{2l + 1} \sum_{m=-l}^{l} |Q_{lm}(i)|^2}. \quad \text{(D3)}$$

In Fig. 16, we show the probability distribution of Q_6 for metallic glass samples of $Cu_{50}Zr_{50}$ prepared using the LJ model at cooling rate $R = 2.6 \times 10^{11}$ K/s and using the EAM model at $R = 1.0 \times 10^{10}$ K/s, as well as disordered FCC samples for both the LJ and EAM models. The thermally quenched LJ and EAM samples possess similar $P(Q_6)$; both are disordered with a peak near $Q_6 \approx 0.12$. $P(Q_6)$ for the disordered FCC systems with LJ interactions is broader than those for the thermally quenched samples and the peak is shifted to $Q_6 \approx 0.15$. $P(Q_6)$ for the disordered FCC systems with EAM interactions has a peak near $Q_6 \approx 0.2$, and it possesses a broad tail that extends beyond $Q_6 \sim 0.5$. Thus, the FCC-initialized systems with EAM interactions include a significant number of crystal-like atoms.

We also characterize the local atomic environment of the metallic glass samples in the numerical simulations using Voronoi indices $(n_3, n_4, n_5, n_6, \ldots)$, where n_i is the number of i-edged faces of a given Voronoi polyhedron. Surfaces with area less than 1% of the total area of the Voronoi polyhedron surfaces are excluded [92]. Icosahedral motifs correspond to polyhedra with Voronoi index $(0,0,12,0)$. Icosahedral motifs can be isolated or occur within linked clusters by sharing a vertex, edge, face, or volume with neighboring icosahedra, as shown in Fig. 17. Linked icosahedra are dominant and their fraction (relative to the total number of icosahedra in
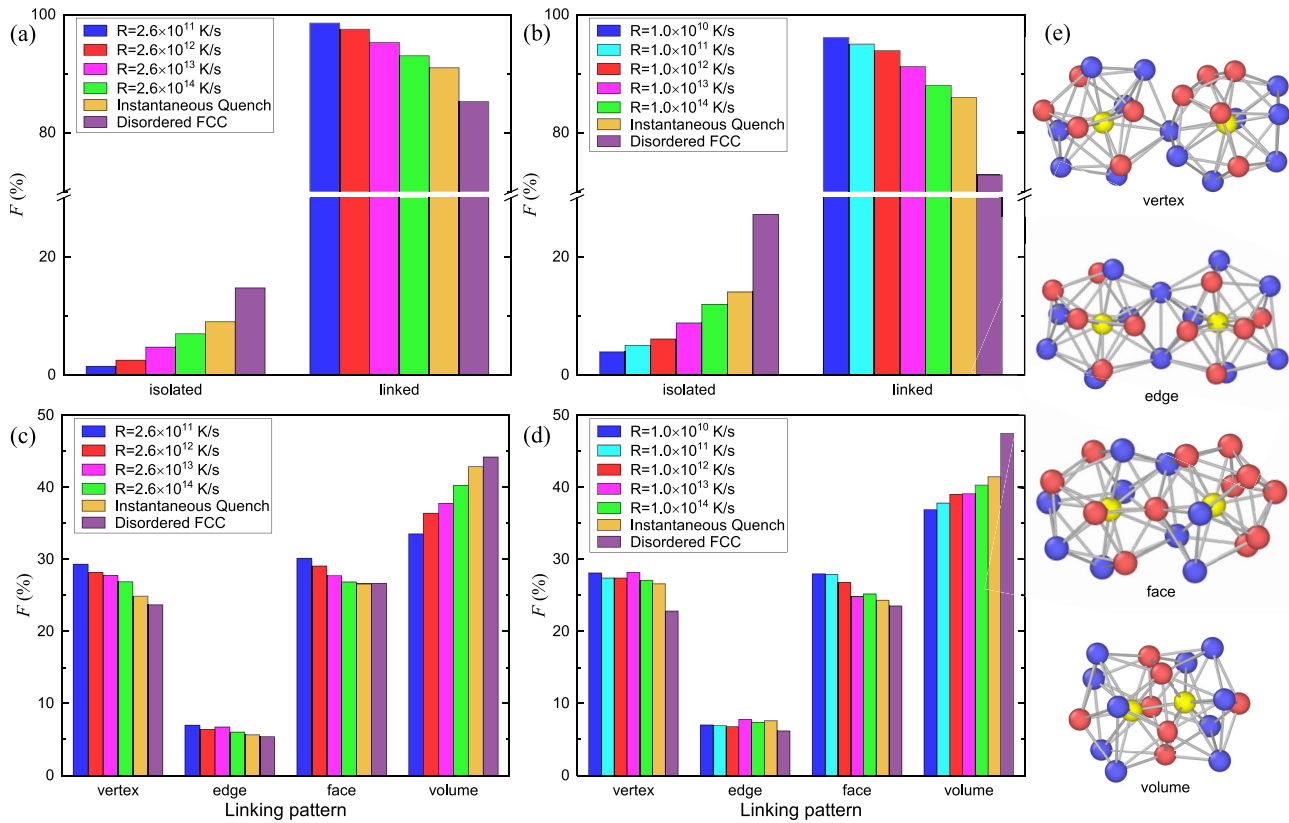
FIG. 17. Fraction of isolated and linked icosahedra for $Cu_{50}Zr_{50}$ metallic glass samples from numerical simulations using the (a) LJ and (b) EAM models. Fraction of icosahedral pairs that share a vertex, edge, face, or volume for the same data in (a) and (b) for the (c) LJ and (d) EAM models. (e) Representative atomic configurations illustrating icosahedral pairs that share a vertex, edge, face, or volume. Central atoms of the icosahedra are colored yellow, and the other atoms are colored blue and red for Cu and Zr atom types, respectively.

samples at each cooling rate) increases with decreasing cooling rate [Figs. 17(a) and 17(b)], while the fraction of icosahedral pairs linked by volume sharing (relative to all linked icosahedra) decreases with decreasing cooling rate [Figs. 17(c) and 17(d)]. Figure 18 shows the icosahe-

dral network formed by volume-sharing icosahedra together with icosahedra-like polyhedra (0,2,8,2) that connect to the neighboring icosahedra via volume sharing. The metallic glass samples generated via slower cooling rates have more icosahedra participating in the icosahedral network. The con-
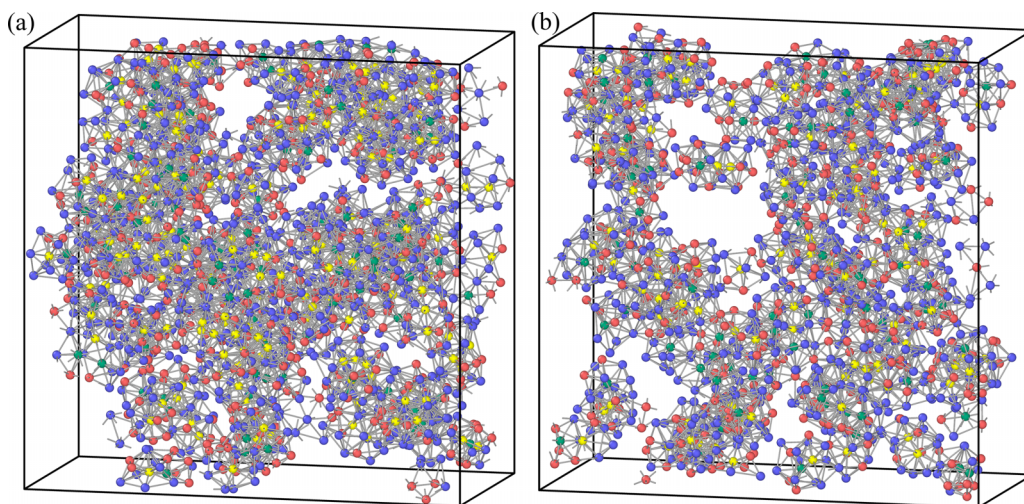

FIG. 18. Snapshots from $Cu_{50}Zr_{50}$ metallic glass samples from numerical simulations of the EAM potential prepared via cooling rates (a) $R = 10^{10}$ and (b) $R = 10^{14}$ K/s that show the spatial distribution of volume-sharing icosahedra together with volume-sharing (0,2,8,2) polyhedra. Volume-sharing icosahedra and (0,2,8,2) polyhedra are colored yellow and green, respectively.
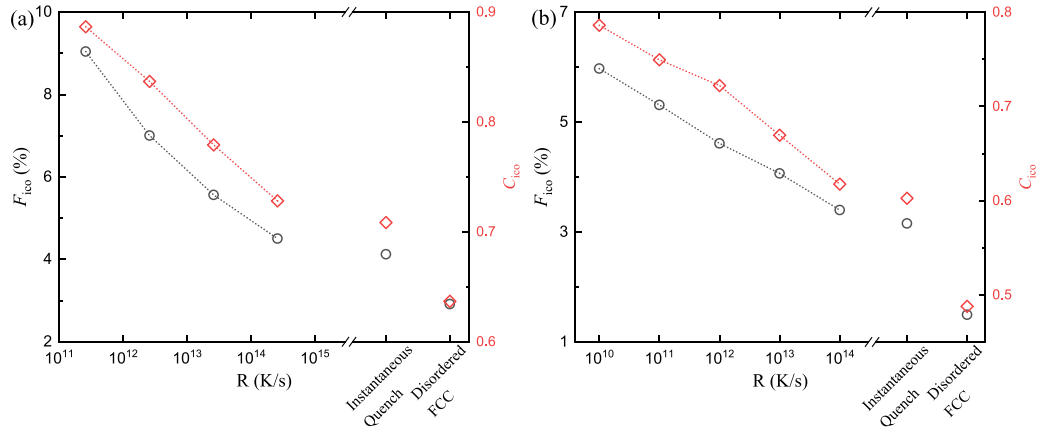
FIG. 19. Fraction (F_{ico}, black circles) and connectivity (C_{ico}, red diamonds) of the icosahedral motifs in $Cu_{50}Zr_{50}$ samples from numerical simulations of the (a) LJ and (b) EAM potentials generated via several preparation protocols.

nectivity of the icosahedral network can be characterized using

$$C_{ico} = \frac{n_I}{N_I}, \tag{D4}$$

where n_I is the number of icosahedral motifs sharing volume with other icosahedra and N_I is the total number of icosahedra [93]. The fraction of icosahedra in a sample is $F_{ico} = n_I/N$, where N is the total number of atoms in the system. Figure 19 shows that the fraction of icosahedral motifs and their connectivity decrease with increasing cooling rate and the disordered FCC structures possess the smallest fraction of icosahedra with the weakest degree of connectivity.

APPENDIX E: SERRATED STRESS VERSUS STRAIN CURVE

In the main text, we calculated the analytical form for $\sigma(\gamma)$ for the spring network model in the $N_s \to \infty$ limit to describe

the ensemble-averaged shear stress versus strain curve from athermal, quasistatic simulations of metallic glasses undergoing tensile loading. For a single configuration, the stress versus strain curve is serrated with short elastic segments punctuated by discontinuous stress drops [24,37,68]. Such serrated stress versus strain relations have been frequently observed in experimental studies of metallic glasses deformed at temperatures below the glass transition temperature and at low strain rates [47–49]. In Fig. 20(a), we calculate the shear stress versus strain for uniaxial tensile loading from the spring network model using a finite number of springs ($N_s = 256$). These results demonstrate that the predictions of the spring network model with a finite number of springs can describe serrated stress versus strain curves. In addition, the spring network model can qualitatively reproduce the distribution of stress drops, as shown in Fig. 20(b), as well as the ensemble-averaged shear stress versus strain behavior.
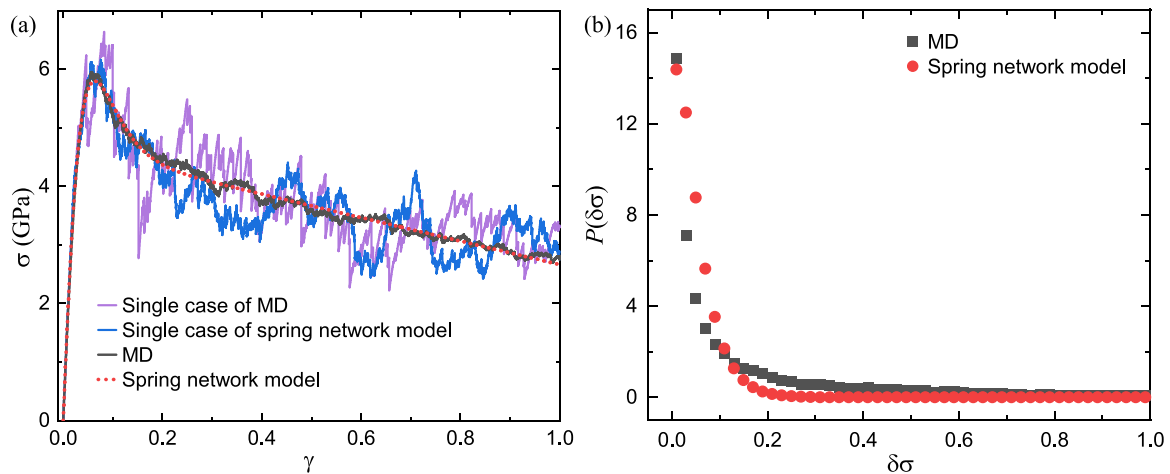

FIG. 20. (a) Engineering stress σ plotted as a function of strain γ for LJ simulations of uniaxial tension of $Cu_{50}Zr_{50}$ metallic glass samples, which are obtained using a cooling rate of 2.6×10^{13} K/s and $N = 3456$. Magenta, blue, black, and red curves denote $\sigma(\gamma)$ from a single MD simulation, a single realization of the spring network model, an average over an ensemble of MD simulations, and the spring network model with $N_s \to \infty$ springs, respectively. (b) Distribution of the stress drops $P(\delta\sigma)$ from the stress vs strain curve obtained from the MD simulations and spring network model in (a).

[1] M. F. Ashby and A. L. Greer, Scr. Mater. **54**, 321 (2006).

[2] C. A. Schuh, T. C. Hufnagel, and U. Ramamurty, Acta Mater. **55**, 4067 (2007).

[3] R. Liontas, M. Jafary-Zadeh, Q. Zeng, Y.-W. Zhang, W. L. Mao, and J. R. Greer, Acta Mater. **118**, 270 (2016).

[4] D. J. Magagnosc, R. Ehrbar, G. Kumar, M. R. He, J. Schroers, and D. S. Gianola, Sci. Rep. **3**, 1096 (2013).

[5] H. Guo, P. F. Yan, Y. B. Wang, J. Tan, Z. F. Zhang, M. L. Sui, and E. Ma, Nat. Mater. **6**, 735 (2007).

[6] L. Tian, Z.-W. Shan, and E. Ma, Acta Mater. **61**, 4823 (2013).

[7] J. Yi, W. H. Wang, and J. J. Lewandowski, Acta Mater. **87**, 1 (2015).

[8] Y. Yokoyama, K. Fujita, A. R. Yavari, and A. Inoue, Philos. Mag. Lett. **89**, 322 (2009).

[9] H. B. Yu, X. Shen, Z. Wang, L. Gu, W. H. Wang, and H. Y. Bai, Phys. Rev. Lett. **108**, 015504 (2012).

[10] Y. Kawamura, T. Shibata, A. Inoue, and T. Masumoto, Scr. Mater. **37**, 431 (1997).

[11] G. Kumar, S. Prades-Rodel, A. Blatter, and J. Schroers, Scr. Mater. **65**, 585 (2011).

[12] G. Kumar, T. Ohkubo, T. Mukai, and K. Hono, Scr. Mater. **57**, 173 (2007).

[13] J. Das, M. B. Tang, K. B. Kim, R. Theissmann, F. Baier, W. H. Wang, and J. Eckert, Phys. Rev. Lett. **94**, 205501 (2005).

[14] F. Shimizu, S. Ogata, and J. Li, Mater. Trans. **48**, 2923 (2007).

[15] D. Rodney, A. Tanguy, and D. Vandembroucq, Modell. Simul. Mater. Sci. Eng. **19**, 083001 (2011).

[16] J. Ding, S. Patinet, M. L. Falk, Y. Cheng, and E. Ma, Proc. Natl. Acad. Sci. USA **111**, 14052 (2014).

[17] A. Zaccone and E. M. Terentjev, J. Appl. Phys. **115**, 033510 (2014).

[18] A. Zaccone, P. Schall, and E. M. Terentjev, Phys. Rev. B **90**, 140203(R) (2014).

[19] D. Şopu, A. Stukowski, M. Stoica, and S. Scudino, Phys. Rev. Lett. **119**, 195503 (2017).

[20] R. Jana and L. Pastewka, J. Phys.: Mater. **2**, 045006 (2019).

[21] M. Wakeda and J. Saida, Sci. Technol. Adv. Mater. **20**, 632 (2019).

[22] A. Barbot, M. Lerbinger, A. Lemaître, D. Vandembroucq, and S. Patinet, Phys. Rev. E **101**, 033001 (2020).

[23] D. Richard, G. Kapteijns, J. A. Giannini, M. L. Manning, and E. Lerner, Phys. Rev. Lett. **126**, 015501 (2021).

[24] W. Jin, A. Datye, U. D. Schwarz, M. D. Shattuck, and C. S. O'Hern, Soft Matter **17**, 8612 (2021).

[25] Z. Zhang, J. Ding, and E. Ma, Proc. Natl. Acad. Sci. USA **119**, e2213941119 (2022).

[26] A. Nicolas, E. E. Ferrero, K. Martens, and J.-L. Barrat, Rev. Mod. Phys. **90**, 045006 (2018).

[27] E. R. Homer and C. A. Schuh, Acta Mater. **57**, 2823 (2009).

[28] L. Li, E. R. Homer, and C. A. Schuh, Acta Mater. **61**, 3347 (2013).

[29] J.-C. Baret, D. Vandembroucq, and S. Roux, Phys. Rev. Lett. **89**, 195506 (2002).

[30] M. Talamali, V. Petäjä, D. Vandembroucq, and S. Roux, Phys. Rev. E **84**, 016115 (2011).

[31] K. Martens, L. Bocquet, and J.-L. Barrat, Soft Matter **8**, 4197 (2012).

[32] G. Zhang, H. Xiao, E. Yang, R. J. S. Ivancic, S. A. Ridout, R. A. Riggleman, D. J. Durian, and A. J. Liu, Phys. Rev. Res. **4**, 043026 (2022).

[33] C. Liu, S. Dutta, P. Chaudhuri, and K. Martens, Phys. Rev. Lett. **126**, 138005 (2021).

[34] D. F. Castellanos, S. Roux, and S. Patinet, Acta Mater. **241**, 118405 (2022).

[35] M. L. Falk and J. S. Langer, Annu. Rev. Condens. Matter Phys. **2**, 353 (2011).

[36] C. Maloney and A. Lemaître, Phys. Rev. Lett. **93**, 195501 (2004).

[37] C. E. Maloney and A. Lemaître, Phys. Rev. E **74**, 016118 (2006).

[38] A. Tanguy, F. Leonforte, and J. L. Barrat, Eur. Phys. J. E **20**, 355 (2006).

[39] A. Tanguy, C. R. Phys. **22**, 117 (2021).

[40] A. Zaccone and E. Scossa-Romano, Phys. Rev. B **83**, 184205 (2011).

[41] M. Baggioli, I. Kriuchevskyi, T. W. Sirk, and A. Zaccone, Phys. Rev. Lett. **127**, 015501 (2021).

[42] M. L. Manning, J. S. Langer, and J. M. Carlson, Phys. Rev. E **76**, 056106 (2007).

[43] A. R. Hinkle, C. H. Rycroft, M. D. Shields, and M. L. Falk, Phys. Rev. E **95**, 053001 (2017).

[44] M. Bletry, P. Guyot, Y. Brechet, J. Blandin, and J. Soubeyroux, Mat. Sci. Eng. A **387-389**, 1005 (2004).

[45] M. Bletry, P. Guyot, J.-J. Blandin, and J.-L. Soubeyroux, Acta Mater. **54**, 1257 (2006).

[46] M. Bletry, P. Guyot, Y. Brechet, J. Blandin, and J.-L. Soubeyroux, Acta Mater. **55**, 6331 (2007).

[47] D. Klaumünzer, R. Maaß, and J. F. Löffler, J. Mater. Res. **26**, 1453 (2011).

[48] R. Ramachandramoorthy, J. Schwiedrzik, L. Petho, C. Guerra-Nunez, D. Frey, J.-M. Breguet, and J. Michler, Nano Lett. **19**, 2350 (2019).

[49] R. Ramachandramoorthy, F. Yang, D. Casari, M. Stolpe, M. Jain, J. Schwiedrzik, J. Michler, J. J. Kruzic, and J. P. Best, J. Mater. Res. **36**, 2325 (2021).

[50] M. J. Alava, P. K. V. V. Nukala, and S. Zapperi, Adv. Phys. **55**, 349 (2006).

[51] P. C. Hemmer and A. Hansen, J. Appl. Mech. **59**, 909 (1992).

[52] S. Pradhan, A. Hansen, and B. K. Chakrabarti, Rev. Mod. Phys. **82**, 499 (2010).

[53] S. Roy, S. Biswas, and P. Ray, Phys. Rev. E **96**, 063003 (2017).

[54] S. Biswas, S. Roy, and P. Ray, Phys. Rev. E **91**, 050105(R) (2015).

[55] Y. Li, Q. Guo, J. A. Kalb, and C. V. Thompson, Science **322**, 1816 (2008).

[56] W. H. Wang, J. J. Lewandowski, and A. L. Greer, J. Mater. Res. **20**, 2307 (2005).

[57] Z. Sha, L. He, S. Xu, Q. Pei, Z. Liu, Y. Zhang, and T. Wang, Scr. Mater. **93**, 36 (2014).

[58] D. Şopu, A. Foroughi, M. Stoica, and J. Eckert, Nano Lett. **16**, 4467 (2016).

[59] H. Song, S. Li, and Q. Deng, Comput. Mater. Sci. **139**, 106 (2017).

[60] H. Heinz, W. Paul, and K. Binder, Phys. Rev. E **72**, 066704 (2005).

[61] R. W. Zwanzig, J. G. Kirkwood, I. Oppenheim, and B. J. Alder, J. Chem. Phys. **22**, 783 (1954).

[62] S. Karmakar, E. Lerner, and I. Procaccia, Phys. Rev. E **82**, 055103(R) (2010).

[63] M. Fan, A. Nawano, J. Schroers, M. D. Shattuck, and C. S. O'Hern, J. Chem. Phys. **151**, 144506 (2019).

[64] P. G. Debenedetti and F. H. Stillinger, Nature (London) **410**, 259 (2001).

[65] X. Yue, C. Liu, S. Pan, A. Inoue, P. Liaw, and C. Fan, Phys. B: Condens. Matter **547**, 48 (2018).

[66] G. Kumar, P. Neibecker, Y. H. Liu, and J. Schroers, Nat. Commun. **4**, 1536 (2013).

[67] J. Ketkaew, W. Chen, H. Wang, A. Datye, M. Fan, G. Pereira, U. D. Schwarz, Z. Liu, R. Yamada, W. Dmowski *et al.*, Nat. Commun. **9**, 3271 (2018).

[68] M. Fan, M. Wang, K. Zhang, Y. Liu, J. Schroers, M. D. Shattuck, and C. S. O'Hern, Phys. Rev. E **95**, 022611 (2017).

[69] C. A. Becker, F. Tavazza, Z. T. Trautt, and R. A. Buarque de Macedo, Curr. Opin. Solid State Mater. Sci. **17**, 277 (2013).

[70] L. M. Hale, Z. T. Trautt, and C. A. Becker, Modell. Simul. Mater. Sci. Eng. **26**, 055003 (2018).

[71] NIST Interatomic Potentials Repository, https://www.ctcms.nist.gov/potentials, Last accessed on 01-17-2023

[72] N. Liu, T. Ma, C. Liao, G. Liu, R. M. O. Mota, J. Liu, S. Sohn, S. Kube, S. Zhao, J. P. Singer, and J. Schroers, Sci. Rep. **11**, 3903 (2021).

[73] P. Bordeenithikasem, J. Liu, S. A. Kube, Y. Li, T. Ma, B. E. Scanley, C. C. Broadbridge, J. J. Vlassak, J. P. Singer, and J. Schroers, Sci. Rep. **7**, 7155 (2017).

[74] S. A. Kube, S. Sohn, D. Uhl, A. Datye, A. Mehta, and J. Schroers, Acta Mater. **166**, 677 (2019).

[75] S. Sato, T. Sanada, J. Saida, M. Imafuku, E. Matsubara, and A. Inoue, Mater. Trans. **46**, 2893 (2005).

[76] Y. H. Li, W. Zhang, C. Dong, J. B. Qiang, A. Makino, and A. Inoue, Intermetallics **18**, 1851 (2010).

[77] M. Ozawa, L. Berthier, G. Biroli, A. Rosso, and G. Tarjus, Proc. Natl. Acad. Sci. USA **115**, 6656 (2018).

[78] M. I. Mendelev, Y. Sun, F. Zhang, C. Z. Wang, and K. M. Ho, J. Chem. Phys. **151**, 214502 (2019).

[79] K. J. Laws, D. B. Miracle, and M. Ferry, Nat. Commun. **6**, 8123 (2015).

[80] C. Kittel, *Introduction to Solid State Physics* (John Wiley & Sons, Hoboken, NJ, 2005).

[81] A. Takeuchi and A. Inoue, Mater. Trans. **46**, 2817 (2005).

[82] D. W. Jacobson and G. B. Thompson, Comput. Mater. Sci. **205**, 111206 (2022).

[83] M. W. Finnis and J. E. Sinclair, Philos. Mag. A **50**, 45 (1984).

[84] C. Tang and P. Harrowell, Nat. Mater. **12**, 507 (2013).

[85] M. L. Falk and J. S. Langer, Phys. Rev. E **57**, 7192 (1998).

[86] P. J. Steinhardt, D. R. Nelson, and M. Ronchetti, Phys. Rev. B **28**, 784 (1983).

[87] M. Leocmach and H. Tanaka, Nat. Commun. **3**, 974 (2012).

[88] Y.-C. Hu, K. Zhang, S. A. Kube, J. Schroers, M. D. Shattuck, and C. S. O'Hern, Phys. Rev. Mater. **4**, 105602 (2020).

[89] C. H. Rycroft, Chaos **19**, 041111 (2009).

[90] W. Mickel, S. C. Kapfer, G. E. Schröder-Turk, and K. Mecke, J. Chem. Phys. **138**, 044501 (2013).

[91] W. Lechner and C. Dellago, J. Chem. Phys. **129**, 114707 (2008).

[92] H. Sheng, W. Luo, F. Alamgir, J. Bai, and E. Ma, Nature (London) **439**, 419 (2006).

[93] M. Lee, C.-M. Lee, K.-R. Lee, E. Ma, and J.-C. Lee, Acta Mater. **59**, 159 (2011).